

A kinetic approach to modeling general-texture evolution in two-dimensional polycrystalline grain growth



I. Yegorov*, M. Emelianenko

George Mason University, Department of Mathematical Sciences, 4400 University Drive, MS: 3F2, Exploratory Hall, Fairfax, VA 22030, USA

ARTICLE INFO

Article history:

Received 24 June 2016

Received in revised form 24 August 2016

Accepted 25 August 2016

Keywords:

Polycrystalline materials

Grain growth

Grain boundary

Energy anisotropy

Cubic lattice symmetry

Disorientation

Number-weighted disorientation

distribution function

Length-weighted disorientation distribution

function

Boltzmann-type kinetic model

ABSTRACT

Important statistical descriptors of grain boundary networks are misorientation distribution functions (often referred to as grain boundary character distributions), which show relative measures of interfaces with given misorientation parameters. This paper is aimed at extending the Boltzmann-type kinetic modeling framework developed in the previous work (Yegorov et al., 2016) to the two-dimensional case of general textures with no restrictions on possible grain orientations, but under the assumption that the grain boundary energy density depends only on the disorientation variable. In order to avoid an enormous computational complexity of treating the general-texture case, the kinetic model for polycrystalline grain growth is constructed from the very beginning in a specific discretized form with respect to the disorientation variable. A significant aspect of the developed approach is that its formulation requires a collection of a priori distributions which describe possible disorientations of grain boundaries connected in a triple junction. A separate numerical algorithm for approximating such distributions is proposed as applied to cubic crystal lattices. The numerical results obtained by the constructed model are in good agreement with the corresponding large-scale simulation results from the related literature.

© 2016 Elsevier B.V. All rights reserved.

1. Introduction

Many technologically useful materials such as metals and ceramics arise as polycrystalline microstructures. They are composed of single crystallites called grains. Interfaces between grains are called grain boundaries. The energetics and connectivity of grain boundary networks are expected to have a direct relationship to many macroscopic properties of materials across all scales of applications. In particular, these include functional properties such as electrical conductivity and lifetime properties like fracture toughness. Engineering of microstructures to achieve desired sets of performance characteristics is a major focus in materials science. An overview of grain boundary engineering was given in [2], and some related applications were discussed in [3–7].

Microstructures, i.e., grains' and grain boundaries' configurations, depend on many physical and chemical factors. In the current paper, the process of microstructural relaxation known as

polycrystalline grain growth is considered. It is characterized by an increase in average size of grains at a high temperature after completion of recovery and recrystallization. In this situation, the further reduction in the interface energy can be reached only by decreasing the total measure of grain boundaries; see, for instance, [8,9].

Important statistical descriptors of grain boundary networks are misorientation distribution functions (often referred to as grain boundary character distributions), which show relative measures of interfaces with given misorientation parameters; see [1,9–24]. In order to investigate how the structure and time evolution of misorientation distribution functions depend on the grain boundary energy anisotropy and set of laws governing the dynamics at a microscopic scale, it is possible to conduct numerical experiments via well-known large-scale simulation approaches. In particular, these are Monte Carlo methods [10–14], phase field models [12,17,18,25], curvature-driven grain growth models [19–21], level set methods [23,24], vertex models [26–28], etc. An alternative way is to develop kinetic models which are based on differential equations and, therefore, can be more computationally efficient, while focusing only on a restricted amount of essential characteristics.

* Corresponding author.

E-mail addresses: ivanyegorov@gmail.com (I. Yegorov), memelian@gmu.edu (M. Emelianenko).

Two novel frameworks for kinetic modeling of anisotropic grain growth with accompanying topological transitions were developed in [14,22]. The paper [22] considered a simplified one-dimensional model and partially adopted a Boltzmann statistical mechanics perspective, which allowed to derive all-sufficient Boltzmann-type kinetic equations. The work [14] proposed a general partial differential equation, covering also two- and three-dimensional grain growth. This equation describes the change in numbers of grain boundaries with particular misorientation parameters as a result of topological transitions. However, all terms in its right-hand side are not known a priori, and, in [14], they were estimated by means of large-scale Monte Carlo simulations. Furthermore, in [14], specific boundary lengthening models were used to connect number-weighted misorientation distribution functions with area-weighted (in a three-dimensional case) or length-weighted (in a two-dimensional case) ones.

The paper [1] modified and combined the two kinetic modeling frameworks from [14,22] as applied to the particular case of polycrystalline thin films with so-called fiber textures. In this sufficiently narrow case, grains have nearly identical orientations in the axial direction perpendicular to a considered film, but random radial orientations in the plane of the film; see also [18]. In comparison with [14], the dependence of the kinetic model on large-scale simulations was essentially decreased. The developed approach has several shortcomings. However, for two nontrivial benchmark examples, its numerical results showed good agreement with the corresponding large-scale simulation results from [18,23]. Also note that the constructed model is not exactly kinetic, because, instead of the time variable, it operates with the time-decreasing total number of grain boundaries.

The current work is aimed at extending the approach developed in [1] to the two-dimensional case of general textures with no restrictions on possible grain orientations, but under the assumption that the grain boundary energy density is a function of a single variable called disorientation. The disorientation of a grain boundary is defined as the smallest rotation angle from all the corresponding symmetrically equivalent misorientations. Although the misorientation of a grain boundary is characterized by three degrees of freedom, such reduction to disorientations is a commonly adopted and reasonable technique; see, for instance, [10,13,14,23,24]. Besides, the two additional variables specifying the orientation of a grain boundary plane are not included in our two-dimensional model, since they are related mainly to three-dimensional grain growth (where a full crystallographic characterization of a grain boundary requires not three but already five degrees of freedom); see [9]. Thus, disorientation distribution functions are the objects of the current investigations.

In order to avoid an enormous computational complexity of treating the general-texture case, the kinetic model is constructed from the very beginning in a specific discretized form with respect to the disorientation variable, as against the fiber-texture considerations in [1].

Moreover, our attention is focused on the symmetry of cubic crystal lattices, because they take place in a wide class of technologically important metals and alloys; see, for instance, [8,29]. A significant aspect of the developed model is that its formulation requires a collection of a priori distributions which describe possible disorientations of grain boundaries connected in a triple junction. A separate numerical algorithm for approximating such distributions is also proposed in the current paper. The structure of the cubic disorientation domain in Rodrigues vector space (see [30,31]) is used in this algorithm.

The developed model is tested by comparing the numerical results, which it gives for several important benchmark examples, with the corresponding large-scale simulation results shown in [14,23].

2. Statement of the problem

Consider two-dimensional grain growth in a polycrystalline thin film with a general texture. Each grain is characterized by a crystallographic orientation which is an orthogonal rotation matrix in the group $SO(3)$. All these orientations are determined in a single fixed three-dimensional Cartesian coordinate system (called sample or specimen coordinate system). We assume that, during growth or shrinkage, grains do not change their orientations.

Adopt the cubic lattice symmetry. Then, for any particular orientation O , there exist exactly 24 equivalent representations or, in other words, crystallographically related solutions. Each of them is generated by premultiplying the matrix O by one of 24 specific matrices $S_j, j = \overline{1, 24}$, called cubic symmetry operators:

$$O_j = S_j \cdot O, \quad j = \overline{1, 24}. \quad (1)$$

Note that the inverse of a cubic symmetry operator and the product of two cubic symmetry operators are also cubic symmetry operators.

Let O' be one of the equivalent orientations for a grain G' , and let O'' be that of another grain G'' . Then the misorientation in the direction from O' to O'' has exactly $24^2 = 576$ equivalent representations

$$M_{jk}^{O', O''} = S_j \cdot O' \cdot (O'')^{-1} \cdot S_k, \quad j = \overline{1, 24}, \quad k = \overline{1, 24}. \quad (2)$$

For every $j = \overline{1, 24}, k = \overline{1, 24}$, consider the axis/angle description corresponding to the matrix $M_{jk}^{O', O''}$ and having the nonnegative rotation angle

$$\theta_{jk}^{O', O''} = \arccos \frac{\text{tr} M_{jk}^{O', O''} - 1}{2} \in [0, \pi] \quad (3)$$

(the opposite angle together with the opposite direction of the rotation axis give an equivalent description). The disorientation angle or, in short, disorientation between O', O'' is defined as the smallest nonnegative rotation angle

$$\theta^{O', O''} = \theta^{O', O'' \text{ def}} = \min_{j=\overline{1, 24}, k=\overline{1, 24}} \theta_{jk}^{O', O''} = \min_{j=\overline{1, 24}, k=\overline{1, 24}} \theta_{jk}^{O', O''}. \quad (4)$$

If G' and G'' are neighboring grains, then the disorientation between G', G'' is interpreted as the disorientation between O', O'' .

The disorientation angle for an arbitrary rotation matrix $R \in SO(3)$ can be determined as

$$\theta^R \stackrel{\text{def}}{=} \min_{j=\overline{1, 24}, k=\overline{1, 24}} \alpha^{S_j \cdot R \cdot S_k} = \min_{j=\overline{1, 24}} \alpha^{S_j \cdot R} = \min_{k=\overline{1, 24}} \alpha^{R \cdot S_k}, \quad (5)$$

where the notation

$$\alpha^Q \stackrel{\text{def}}{=} \arccos \frac{\text{tr} Q - 1}{2} \quad (6)$$

is used for the nonnegative rotation angle in the corresponding axis/angle description of a rotation matrix $Q \in SO(3)$. Indeed, for every $k = \overline{1, 24}, j = \overline{1, 24}$, there exists $l_{kj} \in \{1, 2, \dots, 24\}$ such that $S_k \cdot S_j = S_{l_{kj}}$ and, hence,

$$\begin{aligned} \text{tr}(S_j \cdot R \cdot S_k) &= \text{tr}(S_k \cdot (S_j \cdot R \cdot S_k) \cdot S_k^{-1}) = \text{tr}(S_k \cdot S_j \cdot R) = \text{tr}(S_{l_{kj}} \cdot R), \\ \text{tr}(S_j \cdot R \cdot S_k) &= \text{tr}(S_j^{-1} \cdot (S_j \cdot R \cdot S_k) \cdot S_j) = \text{tr}(R \cdot S_k \cdot S_j) = \text{tr}(R \cdot S_{l_{kj}}). \end{aligned}$$

This implies (5). In particular, we can simplify (4) as

$$\theta^{O', O''} = \theta^{O', O''} = \min_{j=\overline{1, 24}} \alpha^{S_j \cdot O' \cdot (O'')^{-1}} = \min_{k=\overline{1, 24}} \alpha^{O' \cdot (O'')^{-1} \cdot S_k}. \quad (7)$$

For the cubic lattice symmetry, the set of possible disorientations is the line segment $[0, \theta_{\max}]$ with

$$\theta_{\max} \approx 62.8 \cdot \frac{\pi}{180} = 62.8^\circ. \quad (8)$$

A more detailed introduction to the mentioned concepts and their fundamental properties can be found, for instance, in [29–31].

Assume that

$$\gamma : [0, \theta_{\max}] \rightarrow [0, +\infty) \quad (9)$$

is the grain boundary energy density depending only on the disorientation variable, $t \in [0, T]$ is the time variable, and the total number and length of grain boundaries in the considered two-dimensional system are $N(t)$ and $L(t)$, respectively. For every $t \in [0, T]$, introduce the measure densities $N(\cdot, t)$ and $L(\cdot, t)$ supported on the line segment $[0, \theta_{\max}]$ and such that the number and total length of boundaries with disorientations from a Borel set $B \subseteq [0, \theta_{\max}]$ at time t are the integrals $\int_B N(\theta, t) d\theta$ and $\int_B L(\theta, t) d\theta$, respectively. In particular,

$$\int_0^{\theta_{\max}} N(\theta, t) d\theta = N(t), \quad \int_0^{\theta_{\max}} L(\theta, t) d\theta = L(t) \quad \forall t \in [0, T]. \quad (10)$$

Also let $\bar{L}(t)$ be the average boundary length in the whole system, and let $\bar{L}(\theta, t)$ be the average length for a particular disorientation $\theta \in [0, \theta_{\max}]$:

$$\bar{L}(t) \stackrel{\text{def}}{=} \frac{L(t)}{N(t)}, \quad \bar{L}(\theta, t) \stackrel{\text{def}}{=} \frac{L(\theta, t)}{N(\theta, t)} \quad \forall \theta \in [0, \theta_{\max}] \quad \forall t \in [0, T]. \quad (11)$$

Now, according to [1,14,18], introduce the number- and length-weighted disorientation distribution functions (DDFs):

$$\rho_n(\theta, t) \stackrel{\text{def}}{=} \frac{N(\theta, t)}{N(t)}, \quad \rho_l(\theta, t) \stackrel{\text{def}}{=} \frac{L(\theta, t)}{L(t)} \quad \forall \theta \in [0, \theta_{\max}] \quad \forall t \in [0, T]. \quad (12)$$

The length-weighted DDF ρ_l can be referred to as grain boundary character distribution (GBCD); see, for instance, [20]. As in [1,14], from (11) and (12), we obtain

$$\frac{\rho_l(\theta, t)}{\rho_n(\theta, t)} = \frac{\bar{L}(\theta, t)}{\bar{L}(t)} \quad \forall \theta \in [0, \theta_{\max}] \quad \forall t \in [0, T]. \quad (13)$$

As in [1], we do not include such characteristic as the grain boundary mobility (discussed, for instance, in [12,17]) into the constructed model, i.e., mobility isotropy is considered. This assumption is reasonable, since, according to the results of Monte Carlo and phase field simulations of two- and three-dimensional grain growth presented in [12,13,17], misorientation (or disorientation) distribution functions resulting from mobility anisotropy subject to energy isotropy are negligibly different from those developed with both mobility and energy isotropy.

We describe topological transitions accompanying two-dimensional grain growth as either neighbor switchings or grain disappearances; see, for instance, [14,27,28]. Suppose that initial microstructures do not contain two-sided grains and only three-sided grains are allowed to disappear. Then, in particular, transformations of three-sided grains into two-sided grains by neighbor switchings are forbidden, and, therefore, two-sided grains cannot appear. In [1, Section 2], some arguments in favor of this assumption are given.

Let the functions $N_s(t)$ and $N_d(t)$ represent total numbers of neighbor switchings and grain disappearances occurring up to a varying time moment t ($N_s(0) = N_d(0) = 0$). As in [1], we also impose the idealizing assumption that $N(\theta, t), N(t), N_s(t), N_d(t)$ change with time not discretely but continuously.

The main goal of this paper is to develop a method to estimate the number- and length-weighted DDFs (12) for the adopted general-texture case and cubic lattice symmetry. With the help of (13), we reduce the problem of constructing both of them to the problem of constructing ρ_n and the right-hand side of (13);

see also [1,14]. We approximate the number-weighted DDF via a kinetic model extending the fiber-texture approach of [1] and estimate the quotient (13) by means of additional framework.

3. Discretization with respect to the disorientation variable

In order to decrease the computational complexity of the kinetic model for general textures, it is reasonable to discretize the set of possible disorientations from the very beginning.

Take a sufficiently dense grid

$$0 = \theta_0 < \theta_1 < \theta_2 < \dots < \theta_{r-1} < \theta_r = \tilde{\theta}_{\max} \quad (14)$$

on the interval $[0, \tilde{\theta}_{\max}]$ for some constant $\tilde{\theta}_{\max}$ such that

$$\theta_{r-1} < \theta_{\max} < \tilde{\theta}_{\max}. \quad (15)$$

Extend the function (9) from $[0, \theta_{\max}]$ to $[0, \tilde{\theta}_{\max}]$ merely by

$$\gamma(\theta) \stackrel{\text{def}}{=} \gamma(\theta_{\max}) \quad \forall \theta \in (\theta_{\max}, \tilde{\theta}_{\max}]. \quad (16)$$

For every $i = \overline{1, r}$, consider all disorientations from the subinterval $[\theta_{i-1}, \theta_i]$ together, and let the value

$$\gamma_i \stackrel{\text{def}}{=} \gamma(\theta_i^{\text{mid}}) \quad (17)$$

of the grain boundary energy density at the midpoint

$$\theta_i^{\text{mid}} \stackrel{\text{def}}{=} \frac{\theta_{i-1} + \theta_i}{2} \quad (18)$$

represent all its values on $[\theta_{i-1}, \theta_i]$. Furthermore, for any $t \in [0, T]$ and $i = \overline{1, r}$, let the value $\bar{L}(\theta_i^{\text{mid}}, t) / \bar{L}(t)$ of the quotient (13) at the point $(\theta_i^{\text{mid}}, t)$ represent its values at points (θ, t) for all $\theta \in [\theta_{i-1}, \theta_i]$.

Then we can approximate the number- and length-weighted DDFs by the vector-functions $\{\rho_n^i(t)\}_{i=1}^r$ and $\{\rho_l^i(t)\}_{i=1}^r$, respectively, where

$$\begin{aligned} \rho_n^i(t) &\stackrel{\text{def}}{=} \int_{\theta_{i-1}}^{\theta_i} \rho_n(\theta, t) d\theta, \\ \rho_l^i(t) &\stackrel{\text{def}}{=} \frac{\frac{\bar{L}(\theta_i^{\text{mid}}, t)}{\bar{L}(t)} \cdot \rho_n^i(t)}{\sum_{j=1}^r \frac{\bar{L}(\theta_j^{\text{mid}}, t)}{\bar{L}(t)} \cdot \rho_n^j(t)} \end{aligned} \quad (19)$$

$\forall t \in [0, T], \quad i = \overline{1, r}.$

It is obvious that

$$\sum_{i=1}^r \rho_n^i(t) = \sum_{i=1}^r \rho_l^i(t) = 1 \quad \forall t \in [0, T]. \quad (20)$$

Also denote

$$N^i(t) \stackrel{\text{def}}{=} \int_{\theta_{i-1}}^{\theta_i} N(\theta, t) d\theta \quad \forall t \in [0, T], \quad i = \overline{1, r}. \quad (21)$$

Due to (12) and (19), we have

$$N^i(t) = N(t) \cdot \rho_n^i(t) \quad \forall t \in [0, T], \quad i = \overline{1, r}. \quad (22)$$

4. System of kinetic equations for the number-weighted DDF

As in [1], consider four types of possible critical events:

- creation of a grain boundary with a particular disorientation as a result of a neighbor switching;
- removal of a grain boundary with a particular disorientation as a result of a neighbor switching;

- removal of a zero-length grain boundary with a particular disorientation as a result of a grain disappearance;
- removal of a nonzero-length grain boundary with a particular disorientation as a result of a grain disappearance.

For every $t \in [0, T]$ and $i = \overline{1, r}$, adopt the following notations:

- $P_{s,+}^i(t)$ is the probability of lying in the interval $[\theta_{i-1}, \theta_i)$ for the disorientation of a grain boundary created as a result of a neighbor switching at the moment t ;
- $P_{s,-}^i(t)$ is the probability of lying in the interval $[\theta_{i-1}, \theta_i)$ for the disorientation of a grain boundary removed as a result of a neighbor switching at the moment t ;
- $P_{d,1}^i(t)$ is the probability of lying in the interval $[\theta_{i-1}, \theta_i)$ for the disorientation of a grain boundary removed with zero length as a result of a grain disappearance at the moment t ;
- $P_{d,2}^i(t)$ is the probability of lying in the interval $[\theta_{i-1}, \theta_i)$ for the disorientation of a grain boundary removed with nonzero length as a result of a grain disappearance at the moment t .

One can easily see that

$$\sum_{i=1}^r P_{s,+}^i(t) = \sum_{i=1}^r P_{s,-}^i(t) = \sum_{i=1}^r P_{d,1}^i(t) = \sum_{i=1}^r P_{d,2}^i(t) = 1 \quad \forall t \in [0, T]. \quad (23)$$

In Section 6, the introduced probabilities will be expressed in terms of the sought-for number-weighted DDF and some auxiliary a priori distributions discussed in Section 5.

Also let $\lambda(t)$ be the ratio of the neighbor switchings' rate to the grain disappearances' rate at the moment t .

Similarly to [1, Section 3], by starting with the basic relation (an analog of [1, formula (8)])

$$\begin{aligned} N^i(t + \Delta t) - N^i(t) = & \left(P_{s,+}^i(t) - P_{s,-}^i(t) \right) \cdot (N_s(t + \Delta t) - N_s(t)) \\ & - P_{d,1}^i(t) \cdot (N_d(t + \Delta t) - N_d(t)) - P_{d,2}^i(t) \\ & \cdot 2(N_d(t + \Delta t) - N_d(t)), \end{aligned} \quad (24)$$

we can derive the following system of ordinary differential equations for the number-weighted DDF (an analog of [1, formula (11)]):

$$\begin{aligned} \rho_n^i(N) + N \cdot \frac{d\rho_n^i(N)}{dN} = & -\frac{\lambda(N)}{3} \cdot \left(P_{s,+}^i(N) - P_{s,-}^i(N) \right) + \frac{1}{3} \\ & \cdot P_{d,1}^i(N) + \frac{2}{3} \cdot P_{d,2}^i(N) \\ \forall N \in [N_{\min}, N_0], \quad i = \overline{1, r}. \end{aligned} \quad (25)$$

Here

$$N_0 \stackrel{\text{def}}{=} N|_{t=0}, \quad N_{\min} \stackrel{\text{def}}{=} N|_{t=T} \quad (26)$$

are parameters. The initial conditions are taken as

$$\rho_n^i(N_0) = \rho_{n,0}^i, \quad i = \overline{1, r}. \quad (27)$$

The vector $\{\rho_{n,0}^i\}_{i=1}^r$ is a discretized representation of the initial number-weighted DDF. When deriving (25), it is assumed that, when a three-sided grain disappears, only one of its sides is eliminated with zero length. We also consider $N = N(t)$ as a strictly decreasing real-valued function and replace the dependence on t with the dependence on N . Let us write a simple numerical scheme for Cauchy problem (25) and (27):

$$\left\{ \begin{aligned} \rho_n^i(N - \Delta N) = & \rho_n^i(N) + \frac{\Delta N}{N} \cdot \left(\rho_n^i(N) + \right. \\ & \left. + \frac{\lambda(N)}{3} \cdot \left(P_{s,+}^i(N) - P_{s,-}^i(N) \right) - \right. \\ & \left. - \frac{1}{3} \cdot P_{d,1}^i(N) - \frac{2}{3} \cdot P_{d,2}^i(N) \right), \\ & i = \overline{1, r}, \\ \Delta N > 0 \text{ is sufficiently small,} \\ \rho_n^i(N_0) = & \rho_{n,0}^i, \quad i = \overline{1, r}. \end{aligned} \right. \quad (28)$$

5. Auxiliary a priori disorientation distributions

In comparison with the fiber-texture case treated in [1], a substantial difficulty of treating the general-texture case is that some additional quantities are required in order to represent $P_{s,+}^i$, $P_{s,-}^i$, $P_{d,1}^i$, $P_{d,2}^i$, $i = \overline{1, r}$, via $\{\rho_n^i\}_{j=1}^r$. They should describe a priori possible disorientations for a grain boundary which is connected in a triple junction together with two other boundaries having given disorientations.

Let us propose a numerical algorithm to construct the needed quantities as discrete distributions. Namely, for every $i = \overline{1, r}$, $i_1 = \overline{1, r}$, $i_2 = \overline{1, r}$, let η_{i_1, i_2}^i be the probability of lying in the interval $[\theta_{i-1}, \theta_i)$ for the disorientation of a grain boundary which is connected in a triple junction with two other boundaries having disorientations from the intervals $[\theta_{i_1-1}, \theta_{i_1})$ and $[\theta_{i_2-1}, \theta_{i_2})$. It is obvious that

$$\eta_{i_1, i_2}^i = \eta_{i_2, i_1}^i, \quad i = \overline{1, r}, \quad i_1 = \overline{1, r}, \quad i_2 = \overline{1, r}, \quad (29)$$

$$\sum_{i=1}^r \eta_{i_1, i_2}^i = 1, \quad i_1 = \overline{1, r}, \quad i_2 = \overline{1, r}. \quad (30)$$

Here it is convenient to use such alternative descriptors of rotation matrices in $SO(3)$ as unit quaternions and Rodrigues vectors; a very brief introduction to them is given, for instance, in [31].

There is a two-to-one homomorphism between the group of unit quaternions and $SO(3)$. For every $j = \overline{1, 24}$, let $s_j \stackrel{\text{def}}{=} (s_j^0, s_j^1, s_j^2, s_j^3)$ be a unit quaternion corresponding to the cubic symmetry operator S_j and such that $s_j^0 \geq 0$. We can take

$$\left\{ \begin{aligned} s_1 & \stackrel{\text{def}}{=} (1, 0, 0, 0), \quad s_2 \stackrel{\text{def}}{=} (0, 1, 0, 0), \\ s_3 & \stackrel{\text{def}}{=} (0, 0, 1, 0), \quad s_4 \stackrel{\text{def}}{=} (0, 0, 0, 1), \\ s_5 & \stackrel{\text{def}}{=} (0.5, 0.5, 0.5, 0.5), \\ s_6 & \stackrel{\text{def}}{=} (0.5, -0.5, 0.5, 0.5), \\ s_7 & \stackrel{\text{def}}{=} (0.5, 0.5, -0.5, 0.5), \\ s_8 & \stackrel{\text{def}}{=} (0.5, 0.5, 0.5, -0.5), \\ s_9 & \stackrel{\text{def}}{=} (0.5, -0.5, -0.5, 0.5), \\ s_{10} & \stackrel{\text{def}}{=} (0.5, -0.5, 0.5, -0.5), \\ s_{11} & \stackrel{\text{def}}{=} (0.5, 0.5, -0.5, -0.5), \\ s_{12} & \stackrel{\text{def}}{=} (0.5, -0.5, -0.5, -0.5), \\ s_{13} & \stackrel{\text{def}}{=} (v, v, 0, 0), \quad s_{14} \stackrel{\text{def}}{=} (v, -v, 0, 0), \\ s_{15} & \stackrel{\text{def}}{=} (v, 0, v, 0), \quad s_{16} \stackrel{\text{def}}{=} (v, 0, -v, 0), \\ s_{17} & \stackrel{\text{def}}{=} (v, 0, 0, v), \quad s_{18} \stackrel{\text{def}}{=} (v, 0, 0, -v), \\ s_{19} & \stackrel{\text{def}}{=} (0, v, v, 0), \quad s_{20} \stackrel{\text{def}}{=} (0, v, 0, v), \\ s_{21} & \stackrel{\text{def}}{=} (0, 0, v, v), \quad s_{22} \stackrel{\text{def}}{=} (0, -v, v, 0), \\ s_{23} & \stackrel{\text{def}}{=} (0, v, 0, -v), \quad s_{24} \stackrel{\text{def}}{=} (0, 0, v, -v), \\ v & \stackrel{\text{def}}{=} \frac{1}{\sqrt{2}}. \end{aligned} \right. \quad (31)$$

The papers [30,31] present methods for selecting single representations out of sets of symmetrically equivalent misorientations in the unit quaternion and Rodrigues vector spaces. The corresponding selection rules yield representations with minimum non-negative rotation angles, i.e., with disorientation angles, and depend only on the considered symmetry of crystal lattices. Adopt the cubic lattice symmetry. Then, in the Rodrigues vector space, these rules lead to the compact domain

$$D_{\text{fund}} \stackrel{\text{def}}{=} \left\{ (d_1, d_2, d_3) \in \mathbb{R}^3 : \sqrt{2} - 1 \geq d_1 \geq d_2 \geq d_3 \geq 0, \right. \\ \left. d_1 + d_2 + d_3 \leq 1 \right\} \quad (32)$$

which can be called the fundamental zone of misorientations subject to the cubic lattice symmetry. The subset of (32) determined by a fixed rotation angle $\theta \in [0, \pi)$ can be characterized as

$$D_{\text{fund}}^\theta \stackrel{\text{def}}{=} \left\{ (d_1, d_2, d_3) \in \mathbb{R}^3 : \right. \\ 0 \leq d_1 \leq \min \left(\tan \left(\frac{\theta}{2} \right), \sqrt{2} - 1 \right), \\ 0 \leq d_2 \leq \min \left(d_1, \sqrt{\tan^2 \left(\frac{\theta}{2} \right) - d_1^2} \right), \\ d_3 = \sqrt{\tan^2 \left(\frac{\theta}{2} \right) - d_1^2 - d_2^2}, \\ \left. d_3 \leq \min(d_2, 1 - d_1 - d_2) \right\}. \quad (33)$$

We have

$$D_{\text{fund}}^\theta \neq \emptyset \quad \forall \theta \in [0, \theta_{\text{max}}], \\ D_{\text{fund}}^\theta = \emptyset \quad \forall \theta > \theta_{\text{max}}. \quad (34)$$

Also denote

$$D_{\text{fund}}^i \stackrel{\text{def}}{=} \bigcup_{\theta \in [\theta_{i-1}, \theta_i)} D_{\text{fund}}^\theta, \quad i = \overline{1, r}. \quad (35)$$

Note that, for every $i = \overline{1, r}$, an implementation (d_1, d_2, d_3) of a random vector uniformly distributed on the set D_{fund}^i can be generated as follows:

- (1) let θ be an implementation of a random variable with the uniform distribution on the interval $[\theta_{i-1}, \theta_i)$;
- (2) let d_1 be an implementation of a random variable with the uniform distribution on the interval $[0, \min(\tan(\theta/2), \sqrt{2} - 1)]$;
- (3) let d_2 be an implementation of a random variable with the uniform distribution on the interval $[0, \min(d_1, \sqrt{\tan^2(\theta/2) - d_1^2})]$;
- (4) take $d_3 = \sqrt{\tan^2(\theta/2) - d_1^2 - d_2^2}$ if $d_3 \leq \min(d_2, 1 - d_1 - d_2)$, otherwise make another attempt by starting from item 1 again.

The validity of this procedure can be directly verified by the use of (33), (35) and the following elementary result from probability theory (the latter should be applied several times).

Lemma. Let two random vectors $X_1 \in \mathbb{R}^{n_1}$, $X_2 \in \mathbb{R}^{n_2}$ constitute the random vector $(X_1, X_2) \in \mathbb{R}^{n_1+n_2}$ having the uniform distribution on some bounded set $G \subset \mathbb{R}^{n_1+n_2}$ with a positive Lebesgue measure $\text{meas}(G)$ in $\mathbb{R}^{n_1+n_2}$, i.e., the probability density of (X_1, X_2) can be written as

$$p_{(X_1, X_2)}(x) = \begin{cases} \frac{1}{\text{meas}(G)}, & x \in G, \\ 0, & x \in \mathbb{R}^{n_1+n_2} \setminus G. \end{cases}$$

Take a point $x_1 \in \mathbb{R}^{n_1}$ at which the probability density of X_1 does not vanish:

$$p_{X_1}(x_1) = \int_{\mathbb{R}^{n_2}} p_{(X_1, X_2)}(x_1, x_2) dx_2 > 0.$$

Then, at any point $x_2 \in \mathbb{R}^{n_2}$, the conditional probability density of X_2 given the occurrence of the value x_1 of X_1 is determined by

$$p_{X_2|X_1}(x_2|x_1) = \frac{p_{(X_1, X_2)}(x_1, x_2)}{p_{X_1}(x_1)} = \begin{cases} \frac{1}{\text{meas}(G) \cdot p_{X_1}(x_1)}, & (x_1, x_2) \in G, \\ 0, & (x_1, x_2) \in \mathbb{R}^{n_1+n_2} \setminus G, \end{cases}$$

which corresponds to the uniform distribution on the set $\{x_2 \in \mathbb{R}^{n_2} : (x_1, x_2) \in G\}$.

Now we are ready to formulate the desired algorithm.

Step 1. Choose a sufficiently large number $M \in \mathbb{N}$, and, for every $i = \overline{1, r}$, generate M implementations $d^{i,m} \stackrel{\text{def}}{=} (d_1^{i,m}, d_2^{i,m}, d_3^{i,m})$, $m = \overline{1, M}$, of a random vector uniformly distributed on D_{fund}^i (the corresponding procedure was described above).

Step 2. For every $i = \overline{1, r}$, $m = \overline{1, M}$, construct the quaternion

$$q^{i,m} \stackrel{\text{def}}{=} (q_0^{i,m}, q_0^{i,m} \cdot d^{i,m}) \quad (36)$$

with

$$q_0^{i,m} \stackrel{\text{def}}{=} \cos \left(\frac{\theta^{i,m}}{2} \right), \\ \theta^{i,m} \stackrel{\text{def}}{=} 2 \cdot \arctan \sqrt{(d_1^{i,m})^2 + (d_2^{i,m})^2 + (d_3^{i,m})^2}, \quad (37)$$

based on the Rodrigues vector $d^{i,m}$. In fact, there is no need to apply the latter formula to compute the rotation angle $\theta^{i,m}$, because, according to the above-described procedure, $\theta^{i,m}$ is generated first and then used for generating $d_1^{i,m}, d_2^{i,m}, d_3^{i,m}$.

Step 3. Fix arbitrary indices i_1 and $i_2 \geq i_1$ from the set $\{1, 2, \dots, r\}$. Let us show how to approximate the discrete distribution $\{\eta_{i_1, i_2}^i\}_{i=1}^r$. Our aim is to estimate possible disorientations of a grain boundary which is connected in a triple junction with two other boundaries having disorientations from $[\theta_{i_1-1}, \theta_{i_1})$ and $[\theta_{i_2-1}, \theta_{i_2})$. Take the symmetric equivalence into account and consider the following products of quaternions (see Fig. 1):

$$(s_{j_1} \cdot q^{i_1, m_1} \cdot s_{k_1}) \cdot (s_{j_2} \cdot q^{i_2, m_2} \cdot s_{k_2}) = s_{j_1} \cdot q^{i_1, m_1} \cdot s_{l_{k_1 j_2}} \cdot q^{i_2, m_2} \cdot s_{k_2}, \\ m_1 = \overline{1, M}, \quad m_2 = \overline{1, M}, \\ j_1 = \overline{1, 24}, \quad k_1 = \overline{1, 24}, \quad j_2 = \overline{1, 24}, \quad k_2 = \overline{1, 24}. \quad (38)$$

By using matrix representations of rotations, cyclic permutation and similarity invariance of the trace of a matrix, as well as the expression for a rotation angle in terms of the trace of the corresponding rotation matrix, we conclude that, instead of (38), it suffices to consider

$$(s_{j_1})^{-1} \cdot (s_{j_1} \cdot q^{i_1, m_1} \cdot s_{l_{k_1 j_2}} \cdot q^{i_2, m_2} \cdot s_{k_2}) \cdot s_{j_1} = q^{i_1, m_1} \cdot s_{l_{k_1 j_2}} \cdot q^{i_2, m_2} \cdot s_{l_{k_2 j_1}}, \\ m_1 = \overline{1, M}, \quad m_2 = \overline{1, M}, \\ (i_1 - 1) \cdot M + m_1 \leq (i_2 - 1) \cdot M + m_2, \\ j_1 = \overline{1, 24}, \quad k_1 = \overline{1, 24}, \quad j_2 = \overline{1, 24}, \quad k_2 = \overline{1, 24}. \quad (39)$$

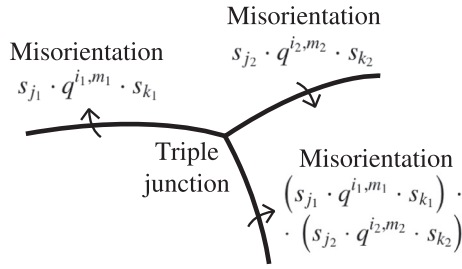


Fig. 1. Misorientations of grain boundaries connected in a triple junction.

In turn, (39) can be characterized in a simpler way:

$$\begin{aligned} & q^{i_1, m_1} \cdot s_j \cdot q^{i_2, m_2} \cdot s_k, \\ & m_1 = \overline{1, M}, \quad m_2 = \overline{1, M}, \\ & (i_1 - 1) \cdot M + m_1 \leq (i_2 - 1) \cdot M + m_2, \\ & j = \overline{1, 2\overline{4}}, \quad k = \overline{1, 2\overline{4}}. \end{aligned} \quad (40)$$

Then we come to the minimum nonnegative rotation angles

$$\begin{aligned} & \min_{k=\overline{1, 2\overline{4}}} (2 \cdot \arccos (q^{i_1, m_1} \cdot s_j \cdot q^{i_2, m_2} \cdot s_k)_0), \\ & m_1 = \overline{1, M}, \quad m_2 = \overline{1, M}, \\ & (i_1 - 1) \cdot M + m_1 \leq (i_2 - 1) \cdot M + m_2, \\ & j = \overline{1, 2\overline{4}}, \end{aligned} \quad (41)$$

where $(q^{i_1, m_1} \cdot s_j \cdot q^{i_2, m_2} \cdot s_k)_0$ is the first component of the quaternion $q^{i_1, m_1} \cdot s_j \cdot q^{i_2, m_2} \cdot s_k$. There are

$$\chi_{i_1, i_2} \stackrel{\text{def}}{=} \begin{cases} 24 \cdot M^2, & i_1 \neq i_2, \\ 24 \cdot \frac{M(M+1)}{2} = 12 \cdot M(M+1), & i_1 = i_2, \end{cases} \quad (42)$$

angles listed in (41); recall that i_1, i_2 are fixed there. For any $i = \overline{1, r}$, let χ_{i_1, i_2}^i denote the number of such angles from (41) that belong to the interval $[\theta_{i-1}, \theta_i)$. It remains to take

$$\eta_{i_2, i_1}^i = \eta_{i_1, i_2}^i \approx \frac{\chi_{i_1, i_2}^i}{\chi_{i_1, i_2}}, \quad i = \overline{1, r}. \quad (43)$$

6. Representations of $P_{s,+}^i, P_{s,-}^i, P_{d,1}^i, P_{d,2}^i, i = \overline{1, r}$

In order to construct representations of $P_{s,+}^i, P_{s,-}^i, P_{d,1}^i, P_{d,2}^i, i = \overline{1, r}$, we develop a modification of the approach proposed in [1, Section 4]. First, let us briefly discuss the main features of the new framework.

1. The fiber-texture considerations in [1, Section 4] allowed to write a direct representation for the misorientation of a grain boundary which is connected in a triple junction together with two other boundaries having given misorientations. In the general-texture case involving disorientation angles, such direct representations cannot be written, and the weights specified by the approximated discrete distributions $\{\eta_{i_1, i_2}^i\}_{i=1}^r, i_1 = \overline{1, r}, i_2 = \overline{1, r}$, have to be used.

2. The representations in [1, Section 4] considered energy dissipation conditions in the sets of integration, i.e., topological transitions leading to an increase of the total grain boundary energy were supposed to be completely impossible. This caused such shortcoming of the developed kinetic model as discontinuities of the number- and length-weighted misorientation distribution functions with respect to the one-dimensional misorientation variable for some important types of grain boundary energy densities.

As in the above-mentioned Monte Carlo techniques, let us consider the probabilities of energy-increasing topological transitions to be nonzero but proportional to an exponentially decaying factor similar to the Boltzmann weight. For this purpose, introduce the function

$$\chi(\gamma_{\text{before}}, \gamma_{\text{after}}) = \begin{cases} 1, & \gamma_{\text{after}} \leq \gamma_{\text{before}}, \\ \exp\left(-\frac{\gamma_{\text{after}} - \gamma_{\text{before}}}{\zeta \cdot \gamma_{\text{before}}}\right), & \gamma_{\text{after}} \geq \gamma_{\text{before}}, \end{cases} \quad (44)$$

where ζ is a positive parameter called effective “lattice temperature” (this is not a real physical temperature); see [13].

3. A significant remark should be added to the previous item. In common with [1, Section 4], we consider a grain disappearance as a combination of two consecutive events. The first one is the neighbor switching which removes one zero-length boundary of a three-sided grain, generates a new zero-length boundary, and binds the remaining two boundaries of the destroyed grain into a two-sided grain. The subsequent event is the instantaneous removal of the generated zero-length boundary together with the whole constructed two-sided grain. Such interpretation is stipulated by the convention that, after a grain disappearance, a new triple junction is located at the first collision point; see, for instance, [28]. Let us treat the first of the mentioned events as described in item 3, and let us not allow the second one to be energy-increasing. Note that the energy dissipation condition for the latter trivially holds when the grain boundary energy density fulfills the triangle inequality introduced in [23]. In particular, Read-Shockley and affine boundary energy densities satisfy this inequality; see [23].

Figs. 2–5 illustrate the four types of events listed in the beginning of Section 4. An index $j \in \{1, 2, \dots, r\}$ written near a grain boundary means that the corresponding disorientation angle belongs to the interval $[\theta_{j-1}, \theta_j)$.

According to Figs. 2–5 (we focus on configurations before critical events) and the foregoing remarks, for all $i = \overline{1, r}$ and $N \in [N_{\min}, N_0]$, we can write

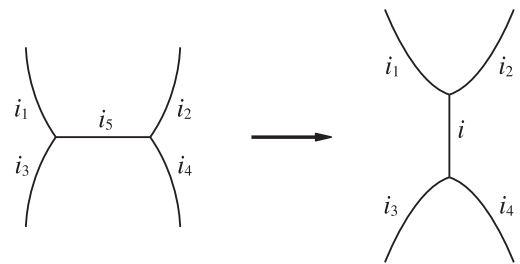


Fig. 2. To formula (46) (creation of a grain boundary with a particular disorientation as a result of a neighbor switching).

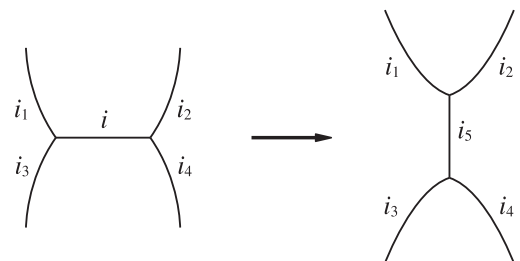


Fig. 3. To formula (47) (removal of a grain boundary with a particular disorientation as a result of a neighbor switching).

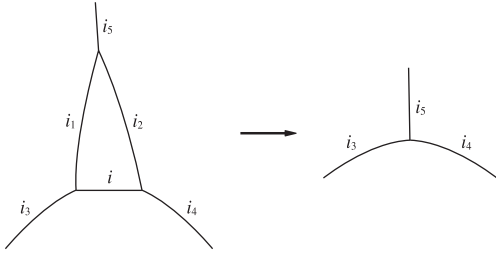


Fig. 4. To formula (48) (removal of a zero-length grain boundary with a particular disorientation as a result of a grain disappearance).

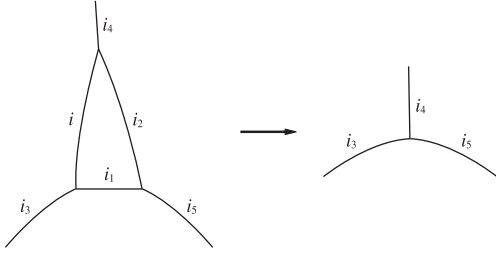


Fig. 5. To formula (49) (removal of a non-zero-length grain boundary with a particular disorientation as a result of a grain disappearance).

$$\begin{aligned}
 P_{s,+}^i(N) &= \frac{p_{s,+}^i(N)}{\sum_{j=1}^r p_{s,+}^j(N)}, \\
 P_{s,-}^i(N) &= \frac{p_{s,-}^i(N)}{\sum_{j=1}^r p_{s,-}^j(N)}, \\
 P_{d,1}^i(N) &= \frac{p_{d,1}^i(N)}{\sum_{j=1}^r p_{d,1}^j(N)}, \\
 P_{d,2}^i(N) &= \frac{p_{d,2}^i(N)}{\sum_{j=1}^r p_{d,2}^j(N)},
 \end{aligned} \tag{45}$$

where

$$\begin{aligned}
 p_{s,+}^i(N) &\stackrel{\text{def}}{=} \eta_{i_1, i_2}^i \cdot \rho_n^{i_1}(N) \cdot \rho_n^{i_2}(N) \\
 &\cdot \sum_{i_5=1}^r \chi(\gamma_{i_5}, \gamma_i) \cdot \rho_n^{i_5}(N) \\
 &\cdot \left(\sum_{i_3=1}^r \eta_{i_5, i_1}^{i_3} \cdot \rho_n^{i_3}(N) \right) \cdot \left(\sum_{i_4=1}^r \eta_{i_5, i_2}^{i_4} \cdot \rho_n^{i_4}(N) \right),
 \end{aligned} \tag{46}$$

$$\begin{aligned}
 p_{s,-}^i(N) &\stackrel{\text{def}}{=} \rho_n^i(N) \cdot \rho_n^{i_1}(N) \cdot \rho_n^{i_2}(N) \\
 &\cdot \left(\sum_{i_3=1}^r \eta_{i_5, i_1}^{i_3} \cdot \rho_n^{i_3}(N) \right) \cdot \left(\sum_{i_4=1}^r \eta_{i_5, i_2}^{i_4} \cdot \rho_n^{i_4}(N) \right) \\
 &\cdot \left(\sum_{i_5=1}^r \eta_{i_1, i_2}^{i_5} \cdot \chi(\gamma_i, \gamma_{i_5}) \right),
 \end{aligned} \tag{47}$$

$$\begin{aligned}
 p_{d,1}^i(N) &\stackrel{\text{def}}{=} \rho_n^i(N) \cdot \rho_n^{i_1}(N) \cdot \rho_n^{i_2}(N) \\
 &\cdot \left(\sum_{i_3=1}^r \eta_{i_5, i_1}^{i_3} \cdot \rho_n^{i_3}(N) \right) \cdot \left(\sum_{i_4=1}^r \eta_{i_5, i_2}^{i_4} \cdot \rho_n^{i_4}(N) \right) \\
 &\cdot \left(\sum_{\substack{i_5 \in \{1, 2, \dots, r\}: \\ \gamma_{i_5} \leq \gamma_{i_1} + \gamma_{i_2}}} \eta_{i_1, i_2}^{i_5} \cdot \chi(\gamma_i, \gamma_{i_5}) \cdot \rho_n^{i_5}(N) \right),
 \end{aligned} \tag{48}$$

$$\begin{aligned}
 p_{d,2}^i(N) &\stackrel{\text{def}}{=} \rho_n^i(N) \cdot \rho_n^{i_1}(N) \cdot \rho_n^{i_2}(N) \\
 &\cdot \left(\sum_{i_3=1}^r \eta_{i_5, i_1}^{i_3} \cdot \rho_n^{i_3}(N) \right) \cdot \left(\sum_{i_5=1}^r \eta_{i_1, i_2}^{i_5} \cdot \rho_n^{i_5}(N) \right) \\
 &\cdot \left(\sum_{\substack{i_4 \in \{1, 2, \dots, r\}: \\ \gamma_{i_4} \leq \gamma_{i_1} + \gamma_{i_2}}} \eta_{i_1, i_2}^{i_4} \cdot \chi(\gamma_{i_1}, \gamma_{i_4}) \cdot \rho_n^{i_4}(N) \right).
 \end{aligned} \tag{49}$$

As in [1,22], we suppose the absence of correlations when writing the right-hand sides of (46)–(49). Besides, one can easily see that, if we denote

$$\gamma_{\max} \stackrel{\text{def}}{=} \max_{\theta \in [0, \theta_{\max}]} \gamma(\theta) \tag{50}$$

and replace γ_j with the normalized value γ_j/γ_{\max} for all $j = \overline{1, r}$, then the quantities (45) will remain the same.

7. Remarks on the model's implementation

1. Since we consider general textures with the cubic lattice symmetry, it is reasonable to take the initial number- and length-weighted DDFs following the well-known Mackenzie distribution. The latter appears when the orientation of every particular grain is chosen randomly in order to have the Euler angles (in Bunge convention)

$$\begin{cases} \varphi_1 = 2\pi r_1, \\ \Phi = \arccos(1 - 2r_2), \\ \varphi_2 = 2\pi r_3, \end{cases} \tag{51}$$

where r_1, r_2, r_3 are independent random numbers generated according to the uniform distribution on the interval $[0, 1]$; see, for instance, [13,14,23,24].

2. Representations (46) and (47) directly imply the relation

$$\sum_{i=1}^r p_{s,+}^i(N) = \sum_{i=1}^r p_{s,-}^i(N) \quad \forall N \in [N_{\min}, N_0], \tag{52}$$

complying with the property that every neighbor switching results in removal of a single boundary and creation of one new boundary; see also [1, Section 5, Remark 2].

3. As in [1, Section 5, Remark 3], we can prove that $\sum_{j=1}^r \rho_n^j(N) = 1$ implies $\sum_{j=1}^r \rho_n^j(N - \Delta N) = 1$ and that the solution to Cauchy problem (25) and (27) should not take negative values if $\rho_{n,0}^j \geq 0, j = \overline{1, r}$, and $\sum_{j=1}^r \rho_{n,0}^j = 1$.

4. Similarly to [1, Section 5, Remark 4], we can transform numerical scheme (28) in order to exclude negative values of an approximate solution to Cauchy problem (25) and (27) which are possible in case of sufficiently large computational inaccuracies. Finally, we come to the following scheme:

$$\begin{cases} \rho_n^i(N - \Delta N) = \\ = \begin{cases} \rho_n^i(N) \cdot e^{A_i(N) \cdot \Delta N} + \frac{B_i(N)}{A_i(N)} \cdot (e^{A_i(N) \cdot \Delta N} - 1), & A_i(N) \neq 0, \\ \rho_n^i(N) + B_i(N) \cdot \Delta N, & A_i(N) = 0, \end{cases} \\ = \rho_n^i(N) \cdot e^{A_i(N) \cdot \Delta N} + B_i(N) \cdot \left(\Delta N + \sum_{k=2}^{\infty} \frac{(A_i(N))^{k-1} \cdot (\Delta N)^k}{k!} \right), \\ A_i(N) \stackrel{\text{def}}{=} \frac{1}{N} \cdot \left(1 - \frac{\lambda(N)}{3} \cdot \frac{P_{s,-}^i(N)}{\rho_n^i(N)} - \frac{1}{3} \cdot \frac{P_{d,1}^i(N)}{\rho_n^i(N)} - \frac{2}{3} \cdot \frac{P_{d,2}^i(N)}{\rho_n^i(N)} \right), \\ B_i(N) \stackrel{\text{def}}{=} \frac{1}{N} \cdot \frac{\lambda(N)}{3} \cdot P_{s,+}^i(N), \\ \Delta N > 0 \text{ is sufficiently small,} \\ \rho_n^i(N_0) = \rho_{n,0}^i. \end{cases} \tag{53}$$

In comparison with (28), the a priori order of accuracy for (53) is at least not lower.

5. For estimating the ratio λ of the neighbor switchings' rate to the grain disappearances' rate, let us use a heuristic method similar to the one proposed in [1, Section 5, Remark 5]. For every $N \in [N_{\min}, N_0]$, introduce the approximate average grain boundary energy density and fractions of low- and high-energy boundaries:

$$\begin{aligned}\bar{\gamma}(N) &\stackrel{\text{def}}{=} \sum_{i=1}^r \gamma_i \cdot \rho_n^i(N), \\ \kappa_{\text{le}}(N) &\stackrel{\text{def}}{=} \sum_{\substack{i \in \{1,2,\dots,r\}: \\ \gamma_i \leq \bar{\gamma}(N)}} \rho_n^i(N), \\ \kappa_{\text{he}}(N) &\stackrel{\text{def}}{=} \sum_{\substack{i \in \{1,2,\dots,r\}: \\ \gamma_i \geq \bar{\gamma}(N)}} \rho_n^i(N) \\ \forall N \in [N_{\min}, N_0].\end{aligned}\quad (54)$$

When $N = N_0$, i.e., $t = 0$, we have

$$\bar{\gamma}_0 \stackrel{\text{def}}{=} \bar{\gamma}(N_0) = \sum_{i=1}^r \gamma_i \cdot \rho_{n,0}^i. \quad (55)$$

Assume that, in the isotropic case when $\gamma_i = \bar{\gamma}_0, i = \overline{1, r}$, the ratio $\lambda = \lambda(N)$ equals some constant $\lambda_{\text{isotr}} > 0$ for all $N \in [N_{\min}, N_0]$. As in [1], we will take $\lambda_{\text{isotr}} \approx 1.34$ according to the results of large-scale numerical simulations presented in [32]. For anisotropic grain boundary energy densities, we estimate λ as

$$\lambda(N) \approx \lambda_{\text{isotr}} \cdot v\left(\frac{2 \cdot \kappa_{\text{he}}(N)}{\kappa_{\text{le}}(N) + \kappa_{\text{he}}(N)}\right) \quad \forall N \in [N_{\min}, N_0], \quad (56)$$

where $v: (0, 2) \rightarrow (0, +\infty)$ is an increasing function such that $v(1) = 1$; for instance, $v(x) = x$ for all $x \in (0, 2)$. We can give the same reasons in favor of this estimate as in [1, Section 5, Remark 5].

8. Boundary lengthening models for estimating the length-weighted DDF

In order to express $\rho_n^i, i = \overline{1, r}$, in terms of $\rho_n^i, i = \overline{1, r}$, via the second equality in (19), where we replace the dependence on t with the dependence on N , let us apply three heuristic quantitative models which describe the mechanism of low-energy boundaries' lengthening at triple junctions. In Section 9, we will compare these models with each other in terms of the obtained numerical results. Also note that the phenomenon of low-energy boundaries' lengthening was justified experimentally; see [16].

Let us denote the considered boundary lengthening models by $\mathbf{L}_1, \mathbf{L}_2, \mathbf{L}_3$. They are stated as follows.

Model \mathbf{L}_1 (see [10,14]):

$$\begin{aligned}\frac{1}{C_1(N)} \cdot \frac{\bar{L}(\theta_i^{\text{mid}}, N)}{\bar{L}(N)} &\approx 1 + c \cdot (1 - \gamma_i) \\ \forall N \in [N_{\min}, N_{\text{interm}}], \quad i &= \overline{1, r}, \\ \text{under the condition that } \gamma_{\text{max}} &= 1, \\ c \approx 6 &\text{ is a suitable constant fitting parameter.}\end{aligned}\quad (57)$$

Model \mathbf{L}_2 (see [1,15]):

$$\begin{aligned}\frac{1}{C_2(N)} \cdot \frac{\bar{L}(\theta_i^{\text{mid}}, N)}{\bar{L}(N)} &\approx \\ \approx \begin{cases} 1 + \frac{1}{2} \left(1 - \frac{\sqrt{3}}{\tan\left(\arccos\left(\frac{\gamma_i}{2\bar{\gamma}(N)}\right)\right)} \right), & \frac{\gamma_i}{\bar{\gamma}(N)} \leq \sqrt{3}, \\ 0, & \frac{\gamma_i}{\bar{\gamma}(N)} \geq \sqrt{3}, \end{cases} \quad (58) \\ \forall N \in [N_{\min}, N_{\text{interm}}], \quad i &= \overline{1, r}.\end{aligned}$$

Model \mathbf{L}_3 (see [14]):

$$\begin{aligned}\frac{1}{C_3(N)} \cdot \frac{\bar{L}(\theta_i^{\text{mid}}, N)}{\bar{L}(N)} &\approx \\ \approx a_0 + a_1 \cdot \frac{\gamma_i}{\gamma_{\text{max}}} + a_2 \cdot \left(\frac{\gamma_i}{\gamma_{\text{max}}}\right)^2 \quad (59) \\ \forall N \in [N_{\min}, N_{\text{interm}}], \quad i &= \overline{1, r}, \\ a_0 = 2.345, \quad a_1 = -1.592, \quad a_2 &= 0.2231.\end{aligned}$$

Here $N_{\text{interm}} \in (N_{\min}, N_0)$ is some constant; for instance, $N_{\text{interm}} = (N_{\min} + N_0)/2$. Its presence is stipulated by the fact that, for anisotropic grain boundary energy densities and the Mackenzie initial number- and length-weighted DDFs (see Remark 1 in Section 7), relations (57)–(59) are not expected to hold at initial stages of texture evolutions. Furthermore, $C_1(N), C_2(N), C_3(N)$ are normalization quantities for all $N \in [N_{\min}, N_{\text{interm}}]$. Nevertheless, after rewriting the right-hand side of the second equality in (19) via any of relations (57)–(59), the normalization quantities cancel each other out in the numerator and denominator. Indeed, (19) automatically implies (20).

According to [10,12,23,25,28], higher-order junctions such as quadruple junctions may become stable in case of highly anisotropic boundary energy densities. The current general-texture framework as well as the fiber-texture framework from [1] do not explicitly operate with stable junctions of orders greater than 3. However, as in [23,28], it is possible to interpret a quadruple junction as two triple junctions connected through a common grain boundary with a relatively small length.

9. Numerical simulations

We adopt the cubic lattice symmetry for which (8) holds. The grid (14) is chosen as follows:

$$\begin{aligned}\theta_i &= i \cdot 2 \cdot \frac{\pi}{180} = i \cdot 2^\circ, \quad i = \overline{0, r}, \quad r = 32, \\ \tilde{\theta}_{\text{max}} &= 64 \cdot \frac{\pi}{180} = 64^\circ.\end{aligned}\quad (60)$$

The a priori distributions $\left\{ \eta_{i_1, i_2}^i \right\}_{i=1}^r, i_1 = \overline{1, r}, i_2 = \overline{1, r}$, are estimated by the use of the algorithm described in Section 5. They have to be constructed only once for the cubic or any other particular lattice symmetry (unlike the number- and length-weighted DDFs depending also on other parameters and initial conditions). The corresponding nonnormalized histograms for several pairs (i_1, i_2) are shown in Fig. 6.

Six types of grain boundary energy densities are considered; see Figs. 7–12.

Type I. Isotropic boundary energy density:

$$\gamma_1(\theta) \stackrel{\text{def}}{=} \gamma_m > 0 \quad \forall \theta \in [0, \theta_{\text{max}}]. \quad (61)$$

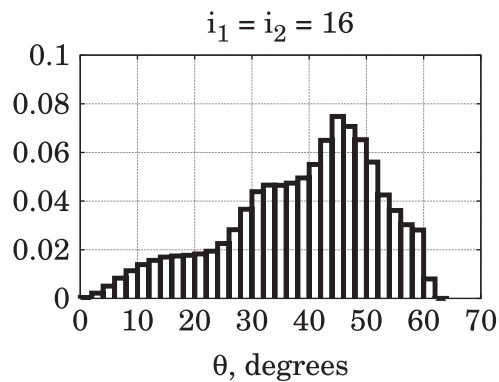
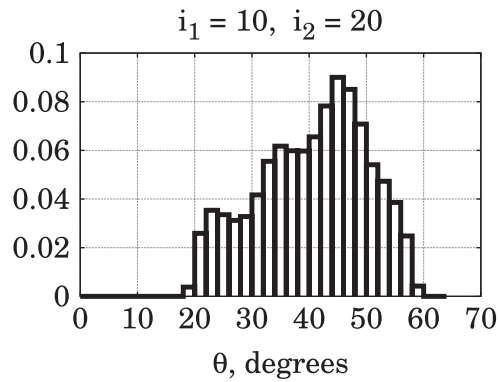
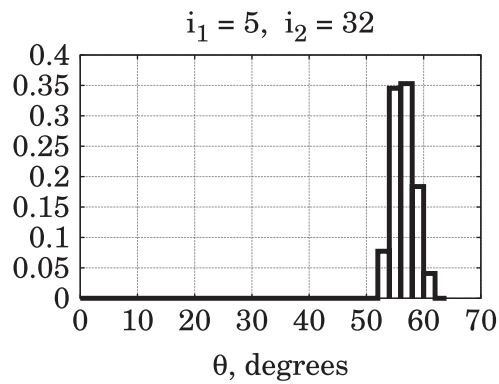
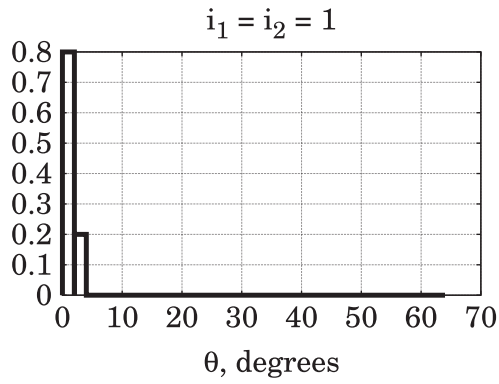


Fig. 6. Nonnormalized histograms for the a priori disorientation distributions corresponding to $\{\eta_{i_1, i_2}^r\}_{i=1}^r$ for different pairs (i_1, i_2) .

Type II. Read-Shockley boundary energy density (see [1,10,13,18,23,24]) with the cutoff angle $\theta_{II} = 15 \cdot \pi/180 = 15^\circ$:

$$\gamma_{II}(\theta) \stackrel{\text{def}}{=} \begin{cases} \gamma_l, & \theta = 0, \\ \gamma_l + (\gamma_m - \gamma_l) \cdot \frac{\theta}{\theta_{II}} \cdot \left(1 - \ln\left(\frac{\theta}{\theta_{II}}\right)\right), & \theta \in (0, \theta_{II}], \\ \gamma_m, & \theta \geq \theta_{II}, \end{cases} \quad (62)$$

$\forall \theta \in [0, \theta_{\max}]$,
 $\gamma_l \in [0, \gamma_m)$.

Type III. Read-Shockley boundary energy density with the cut-

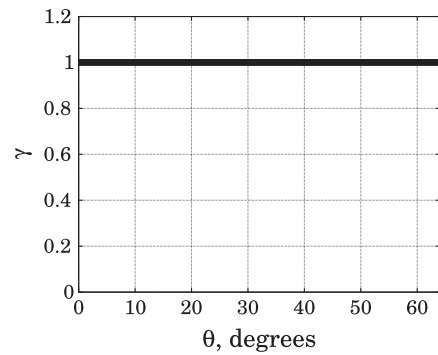


Fig. 7. Grain boundary energy density of Type I.

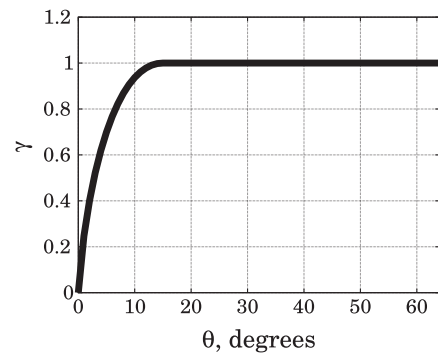


Fig. 8. Grain boundary energy density of Type II.

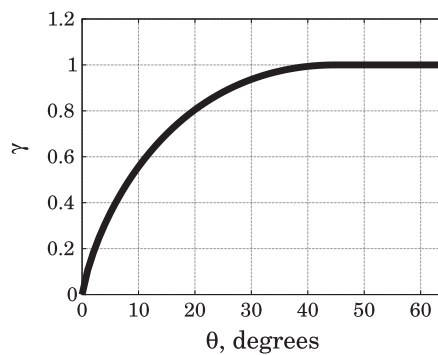


Fig. 9. Grain boundary energy density of Type III.

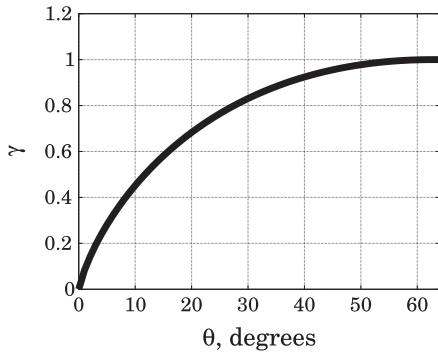


Fig. 10. Grain boundary energy density of Type IV.

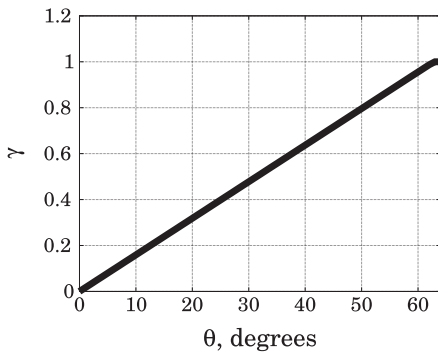


Fig. 11. Grain boundary energy density of Type V.

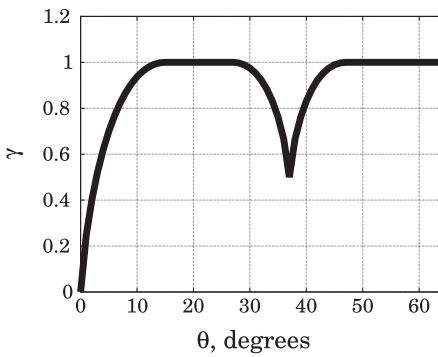


Fig. 12. Grain boundary energy density of Type VI.

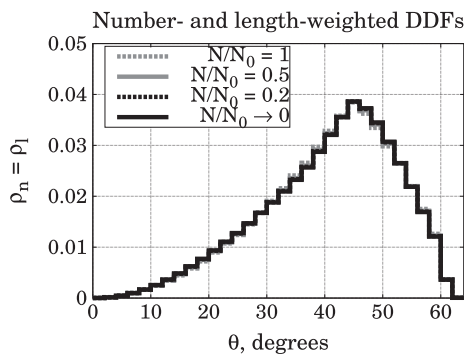


Fig. 13. Normalized histograms approximating the number- and length-weighted DDFs for the grain boundary energy density of Type I and $\lambda = \lambda(N)$ determined by (56) with $\lambda_{isotr} = 1.34$, $v(x) \equiv x$.

off angle $\theta_{III} = 45 \cdot \pi/180 = 45^\circ$: $\gamma_{III} = \gamma_{III}(\theta)$ is defined by (62) if we replace θ_{II} with θ_{III} there.

Type IV. Read-Shockley boundary energy density with the cut-off angle $\theta_{IV} = \theta_{max} \approx 62.8 \cdot \pi/180 = 62.8^\circ$: $\gamma_{IV} = \gamma_{IV}(\theta)$ is defined by (62) if we replace θ_{II} with θ_{IV} there.

Type V. Affine boundary energy density (see [23]):

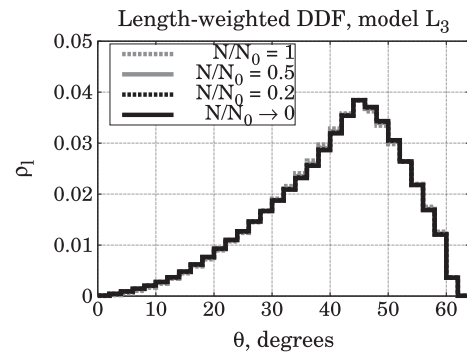
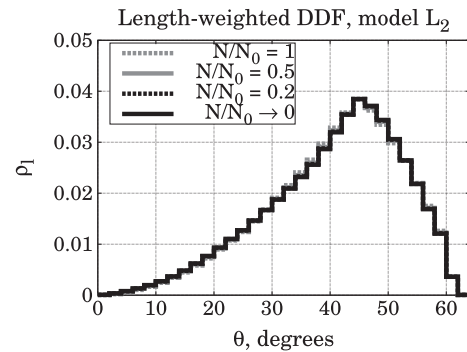
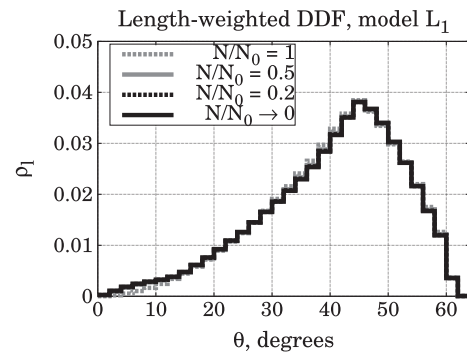
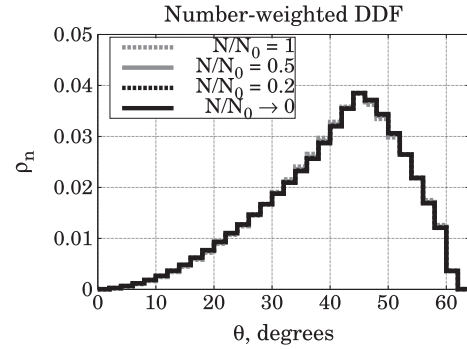


Fig. 14. Normalized histograms approximating the number- and length-weighted DDFs for the grain boundary energy density of Type II and $\lambda = \lambda(N)$ determined by (56) with $\lambda_{isotr} = 1.34$, $v(x) \equiv x$. Three different boundary lengthening models L_1 , L_2 , L_3 for representing the length-weighted DDF in terms of the number-weighted DDF are implemented.

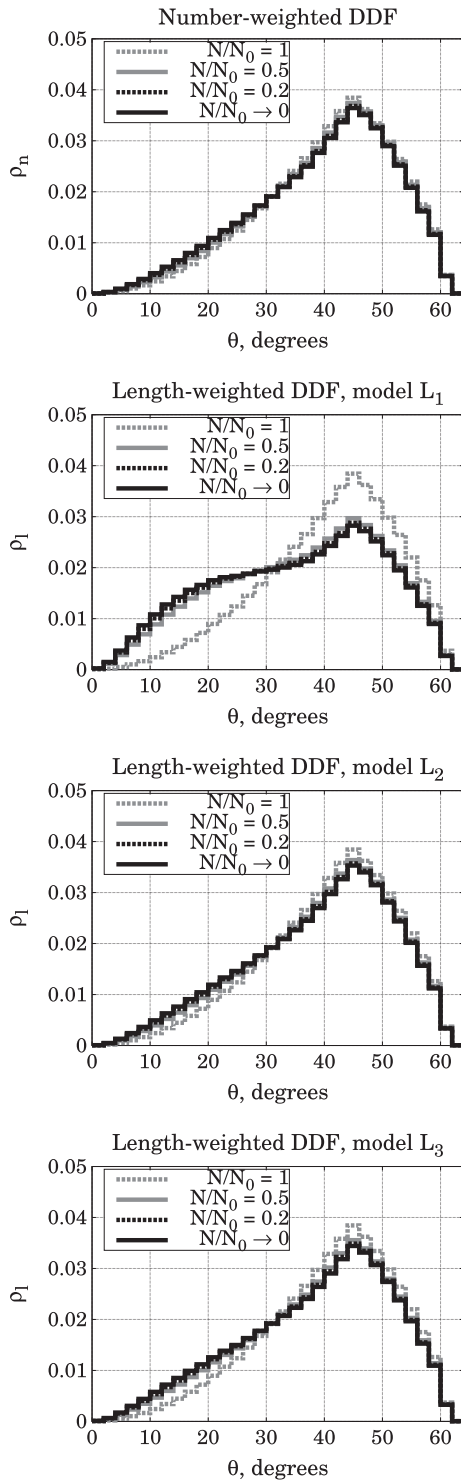


Fig. 15. Normalized histograms approximating the number- and length-weighted DDFs for the grain boundary energy density of Type III and $\lambda = \lambda(N)$ determined by (56) with $\lambda_{\text{isotr}} = 1.34$, $v(x) \equiv x$. Three different boundary lengthening models L_1 , L_2 , L_3 for representing the length-weighted DDF in terms of the number-weighted DDF are implemented.

$$\gamma_V(\theta) \stackrel{\text{def}}{=} \gamma_l + (\gamma_m - \gamma_l) \cdot \frac{\theta}{\theta_{\max}} \quad \forall \theta \in [0, \theta_{\max}]. \quad (63)$$

Type VI. Modification of γ_{II} with an additional local minimum (see [1,18]):

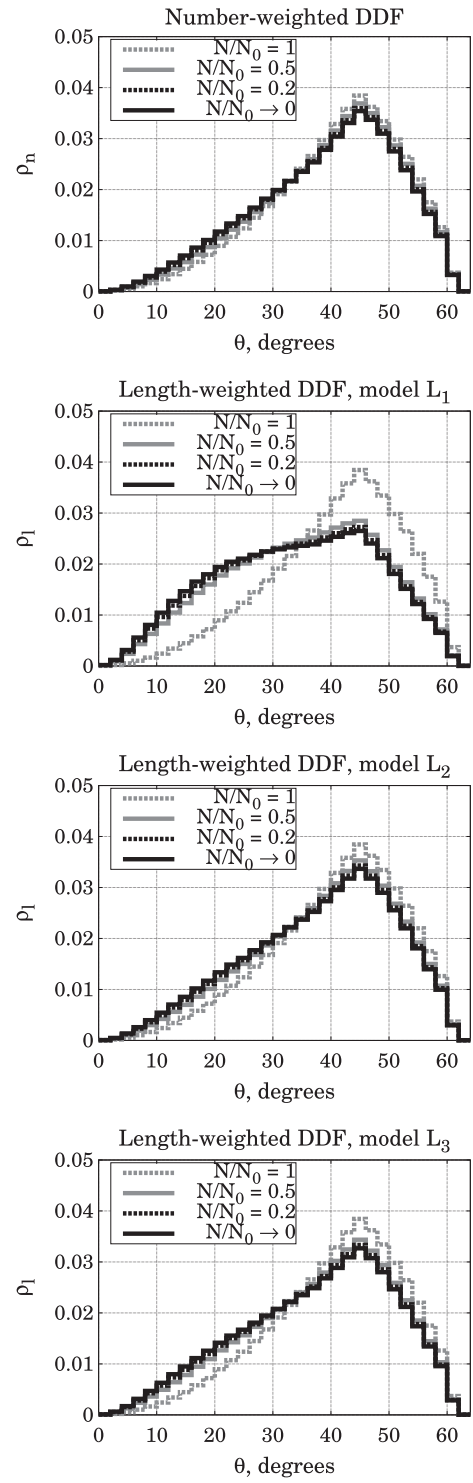


Fig. 16. Normalized histograms approximating the number- and length-weighted DDFs for the grain boundary energy density of Type IV and $\lambda = \lambda(N)$ determined by (56) with $\lambda_{\text{isotr}} = 1.34$, $v(x) \equiv x$. Three different boundary lengthening models L_1 , L_2 , L_3 for representing the length-weighted DDF in terms of the number-weighted DDF are implemented.

$$\gamma_{VI}(\theta) \stackrel{\text{def}}{=} \begin{cases} \gamma_{II}(\theta), & \theta \in [0, \theta_{VI} - \theta'_{VI}], \\ \gamma_{l,1} + (\gamma_m - \gamma_{l,1}) \cdot \frac{|\theta - \theta_{VI}|}{\theta'_{VI}}, & \theta \in [\theta_{VI} - \theta'_{VI}, \theta_{VI} + \theta'_{VI}] \setminus \{\theta_{VI}\}, \\ \gamma_{l,1}, & \theta = \theta_{VI}, \\ \gamma_m, & \theta \geq \theta_{VI} + \theta'_{VI}, \end{cases} \quad (64)$$

$\forall \theta \in [0, \theta_{\max}]$,
 $\gamma_{l,1} \in (\gamma_l, \gamma_m)$, $\theta_{VI} \in (\theta_{II}, \theta_{\max}]$, $\theta'_{VI} \in (0, \theta_{VI} - \theta_{II}]$.

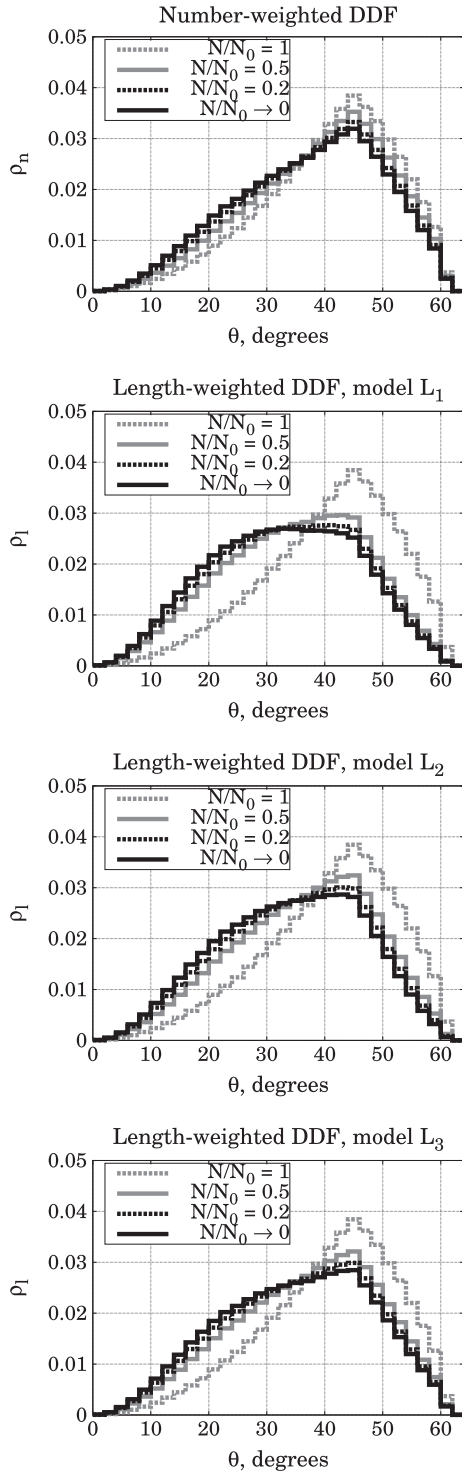


Fig. 17. Normalized histograms approximating the number- and length-weighted DDFs for the grain boundary energy density of Type **V** and $\lambda = \lambda(N)$ determined by (56) with $\lambda_{\text{isotr}} = 1.34$, $v(x) \equiv x$. Three different boundary lengthening models **L**₁, **L**₂, **L**₃ for representing the length-weighted DDF in terms of the number-weighted DDF are implemented.

Here we take $\theta_{\text{VI}} = 37 \cdot \pi/180 = 37^\circ$, $\theta'_{\text{VI}} = 10 \cdot \pi/180 = 10^\circ$, $\gamma_{l,1} = (\gamma_l + \gamma_m)/2$.

It is obvious that, for any fixed constant $C > 0$, replacing $\gamma(\theta)$ with $C \cdot \gamma(\theta)$ does not change our approximations of $\{\rho_n^i(N)\}_{i=1}^r$, $\{\rho_l^i(N)\}_{i=1}^r$. Let us choose $\gamma_l = 0$, $\gamma_m = 1$.

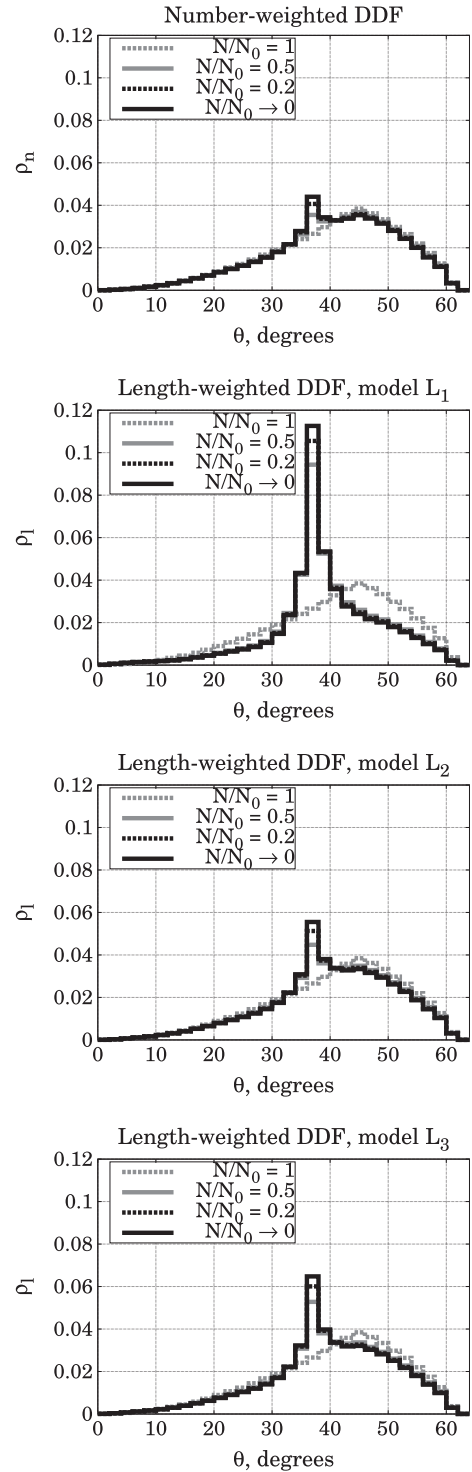


Fig. 18. Normalized histograms approximating the number- and length-weighted DDFs for the grain boundary energy density of Type **VI** and $\lambda = \lambda(N)$ determined by (56) with $\lambda_{\text{isotr}} = 1.34$, $v(x) \equiv x$. Three different boundary lengthening models **L**₁, **L**₂, **L**₃ for representing the length-weighted DDF in terms of the number-weighted DDF are implemented.

In conformity with [13, Section 2.2], the effective “lattice temperature” is taken as $\zeta = 0.7$ for two-dimensional simulations.

We set $N_0 = 300000$. This is reasonable if the initial number of grains is 100000 and the initial average number of sides per grain is 6, because each grain boundary belongs to exactly two grains; see, for instance, [9, Section 4.6.2]. According to Remark 1 in

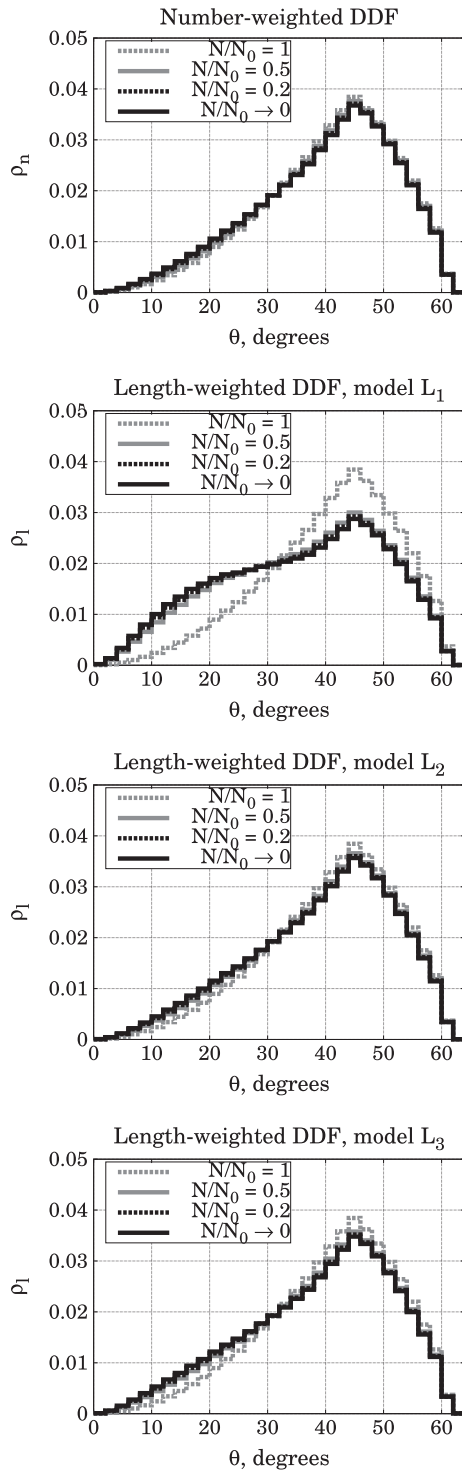


Fig. 19. Normalized histograms approximating the number- and length-weighted DDFs for the grain boundary energy density of Type III and $\lambda(N) \equiv 1.34$. Three different boundary lengthening models L_1 , L_2 , L_3 for representing the length-weighted DDF in terms of the number-weighted DDF are implemented.

Section 7, $\{\rho_{n,0}^i\}_{i=1}^r = \{\rho_n^i(N_0)\}_{i=1}^r$ and $\{\rho_{l,0}^i\}_{i=1}^r = \{\rho_l^i(N_0)\}_{i=1}^r$ follow the nonnormalized histograms for Mackenzie distribution on the disorientation grid (60). In order to compute $\{\rho_n^i(N)\}_{i=1}^r$, we use numerical scheme (53) with $\Delta N = N_0/600 = 500$ step-by-step till the very end $N_{\min} = 0$ at which $\{\rho_n^i\}_{i=1}^r|_{N=0}$ is obtained by

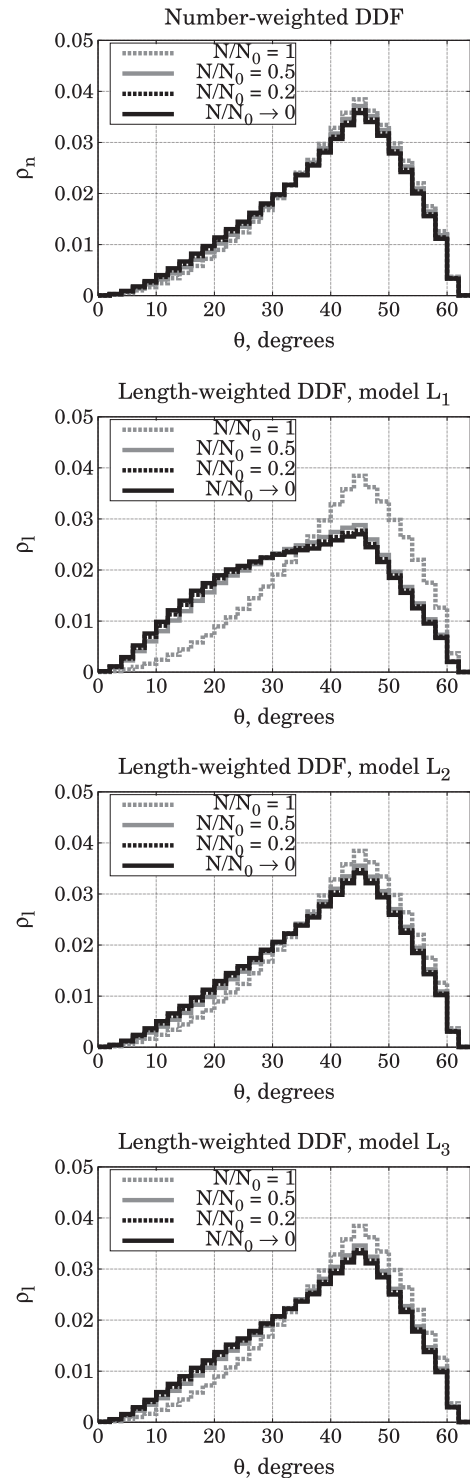


Fig. 20. Normalized histograms approximating the number- and length-weighted DDFs for the grain boundary energy density of Type IV and $\lambda(N) \equiv 1.34$. Three different boundary lengthening models L_1 , L_2 , L_3 for representing the length-weighted DDF in terms of the number-weighted DDF are implemented.

means of $\{\rho_n^i\}_{i=1}^r|_{N=\Delta N}$. After approximating $\{\rho_n^i(N)\}_{i=1}^r$, we apply (57)–(59) with $N_{\text{interm}} = N_0/2 = 150000$ so as to estimate $\{\rho_l^i(N)\}_{i=1}^r$ from $N = N_{\text{interm}}$ to $N = 0$.

As in [1], we consider the following two ways of determining the ratio $\lambda = \lambda(N)$ of the neighbor switchings' rate to the grain disappearances' rate (see remark 5 in Section 7 and recall that the value $\lambda_{\text{isotr}} = 1.34$ is taken from [32]):

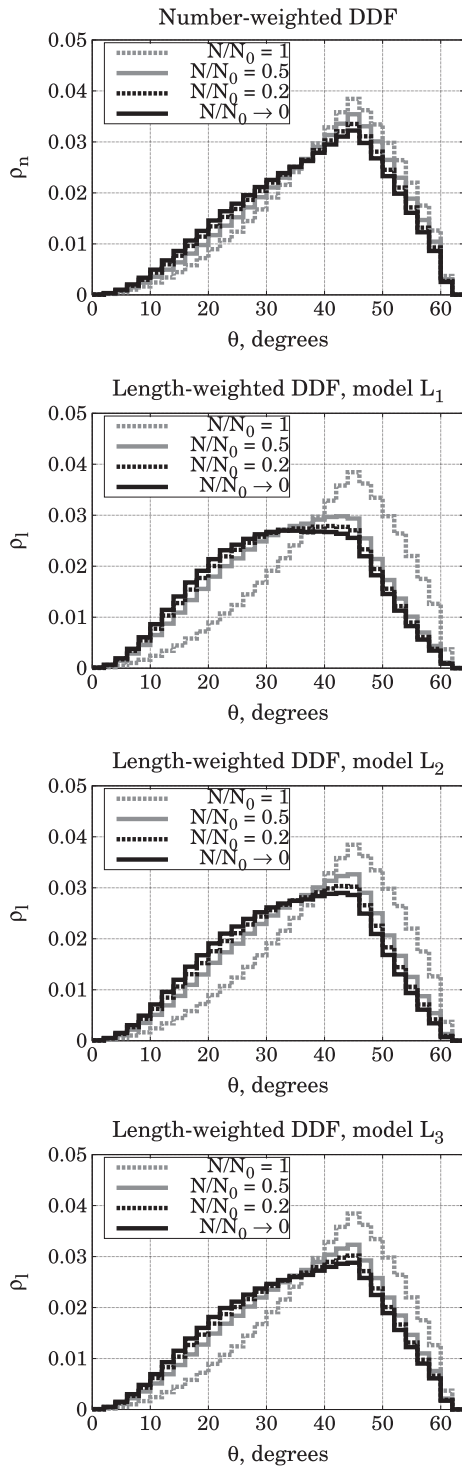


Fig. 21. Normalized histograms approximating the number- and length-weighted DDFs for the grain boundary energy density of Type **V** and $\lambda(N) \equiv 1.34$. Three different boundary lengthening models **L₁**, **L₂**, **L₃** for representing the length-weighted DDF in terms of the number-weighted DDF are implemented.

- (A) $\lambda(N) \equiv 1.34$;
- (B) $\lambda = \lambda(N)$ is estimated according to (56) with $\lambda_{\text{isotr}} = 1.34$ and $v(x) \equiv x$.

Nevertheless, we will focus on case **B**, because it is nontrivial and, as will be seen in several examples below, there is only a slight difference between cases **A,B** in terms of the constructed

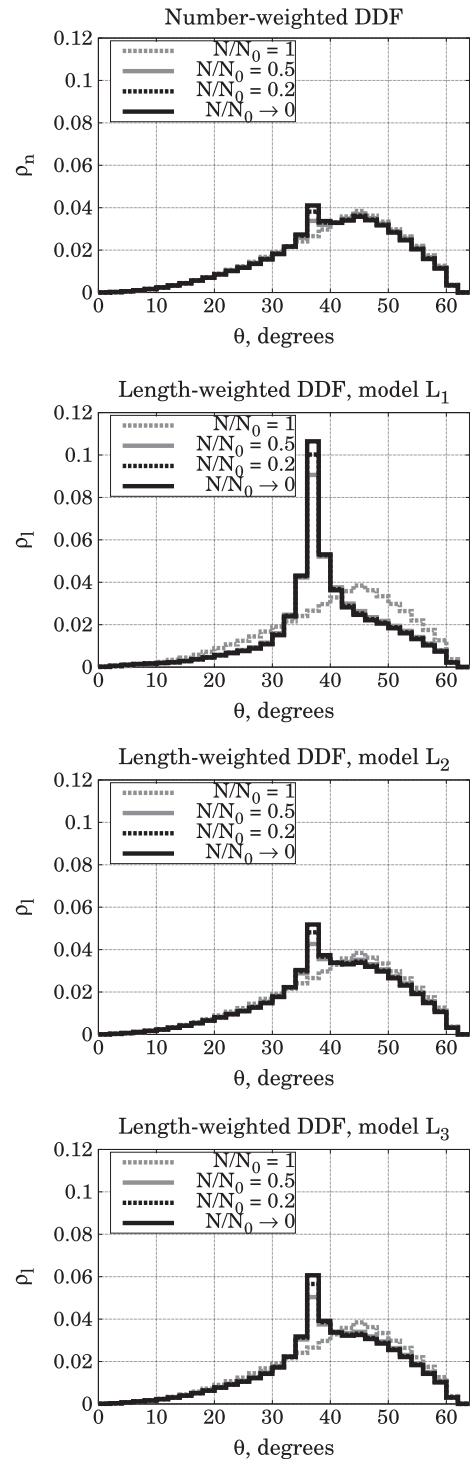


Fig. 22. Normalized histograms approximating the number- and length-weighted DDFs for the grain boundary energy density of Type **VI** and $\lambda(N) \equiv 1.34$. Three different boundary lengthening models **L₁**, **L₂**, **L₃** for representing the length-weighted DDF in terms of the number-weighted DDF are implemented.

approximations of the number- and length-weighted DDFs; also recall [1, Section 5, the end of Remark 5].

Figs. 13–22 show the evolving normalized histograms based on $\{\rho_n^i(N)\}_{i=1}^r$ and on the three variants of $\{\rho_l^i(N)\}_{i=1}^r$ estimated via boundary lengthening models **L₁**, **L₂**, **L₃**. In Figs. 13–18, case **B** is illustrated for all the considered types of boundary energy densities. The numerical results in case **A** turn out to be negligibly

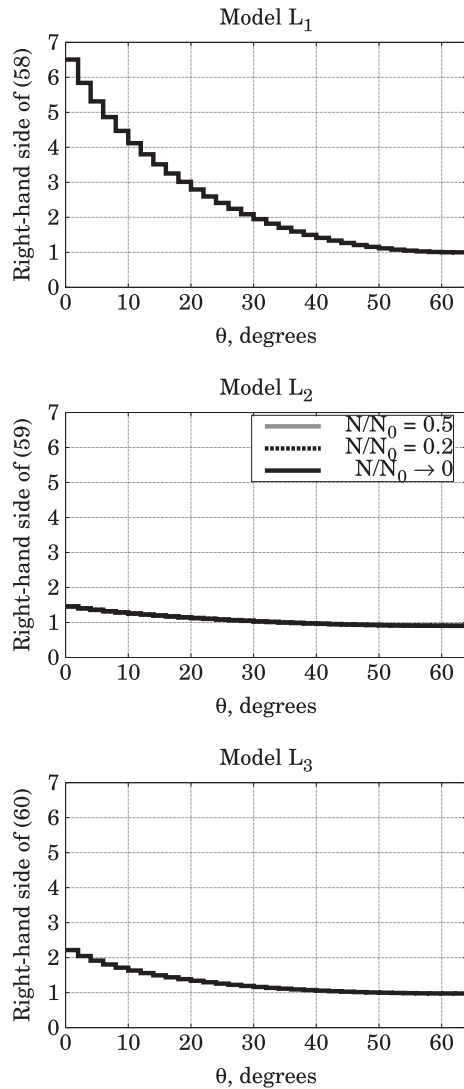


Fig. 23. Right-hand sides of (57)–(59) (specifying boundary lengthening models L_1 , L_2 , L_3) for the grain boundary energy density of Type IV. The right-hand side of (58) is computed for the case when $\lambda = \lambda(N)$ is determined by (56) with $\lambda_{\text{isotr}} = 1.34$, $v(x) \equiv x$.

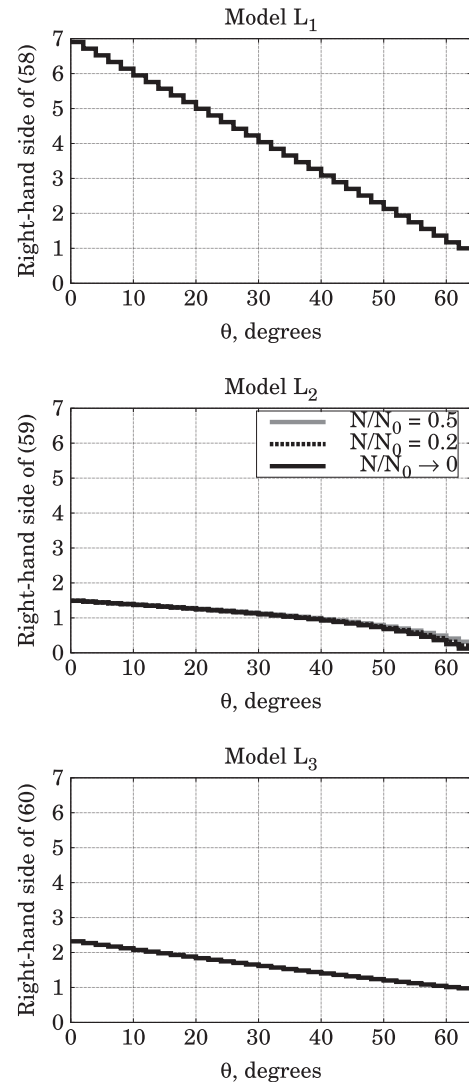


Fig. 24. Right-hand sides of (57)–(59) (specifying boundary lengthening models L_1 , L_2 , L_3) for the grain boundary energy density of Type V. The right-hand side of (58) is computed for the case when $\lambda = \lambda(N)$ is determined by (56) with $\lambda_{\text{isotr}} = 1.34$, $v(x) \equiv x$.

different from those in case **B**. For the boundary energy densities of Types **III–VI**, one can directly see this by comparing Figs. 15–18 with Figs. 19–22, respectively. For the boundary energy densities of Types **I,II**, there is almost no evolution (as follows from Figs. 13 and 14), and the similarity between the portraits in cases **A,B** is even more evident; the corresponding figures for case **A** are omitted for the sake of brevity.

Figs. 23–25 illustrate the graphs of the right-hand sides of representations (57)–(59) (specifying boundary lengthening models L_1, L_2, L_3) for the boundary energy densities of Types **IV–VI**. The right-hand side of (58) depending on the average boundary energy density $\bar{\gamma}(N)$ as well as on the disorientation variable θ is computed for case **B**.

Figs. 26–29 show the evolving normalized histograms based on $\{P_{s,+}^i(N)\}_{i=1}^r$, $\{P_{s,-}^i(N)\}_{i=1}^r$, $\{P_{d,1}^i(N)\}_{i=1}^r$, $\{P_{d,2}^i(N)\}_{i=1}^r$ and graphs of the functions (54) and (56) for the boundary energy densities of Types **II,VI** and case **B**.

In addition to the mentioned similarity of cases **A,B**, the following principal conclusions can be drawn from the presented simulation results.

1. With the help of the factor (44), we have avoided unnatural jumps of the approximated number- and length-weighted DDFs at cutoff disorientation angles; see Figs. 14–16, 18–20, 22. Such jumps do not appear in the large-scale simulation results demonstrated in [13,18,23] and, therefore, constitute a shortcoming of the model developed in [1].

2. Figs. 13–16, 19, 20 indicate that, for the boundary energy densities of Types **I–IV**, the number-weighted DDF evolves negligibly and do not differ substantially from Mackenzie distribution. This conforms with the Monte Carlo simulation results shown in [13, Fig. 5(a)]. From Figs. 17, 18, 21 and 22 concerning the boundary energy densities of Types **V,VI**, we observe a noticeable increase in the number-weighted DDF on some of low-energy disorientation intervals. However, this increase is much weaker than in the fiber-texture case, where large peaks of misorientation distributions appear at points of local and global energy minima; see [18,1]. Thus, the geometric restrictions related to the general-texture case and specified by the a priori distributions $\{\eta_{i_1, i_2}^i\}_{i=1}^r$, $i_1 = \overline{1, r}$, $i_2 = \overline{1, r}$ (see Fig. 6), do not allow grain boundaries with low disorientation angles to be created in large amounts

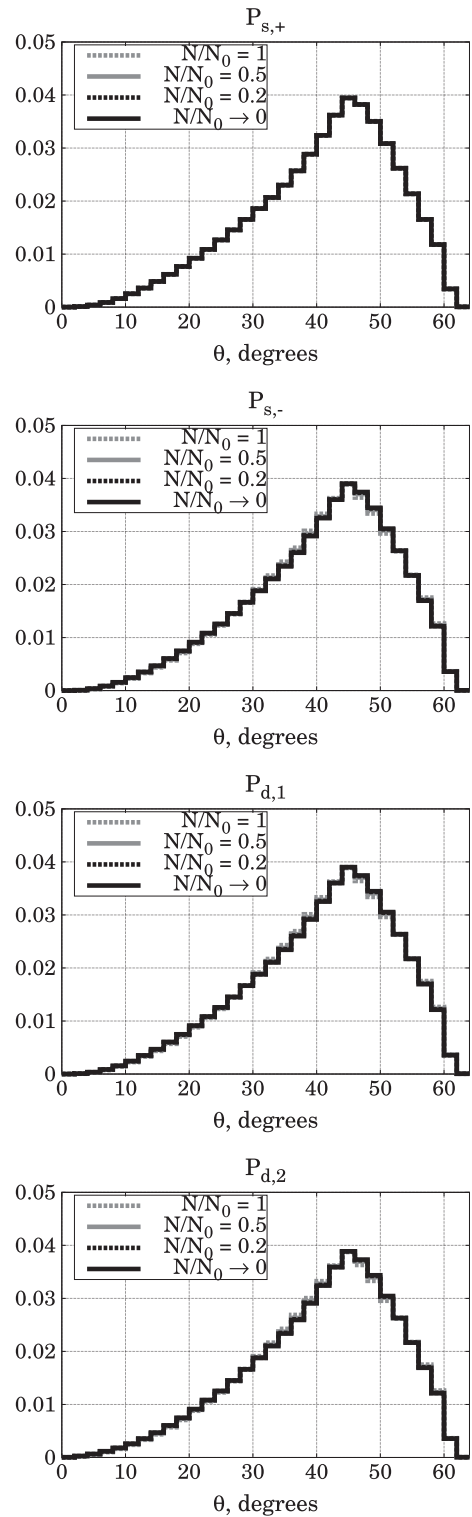
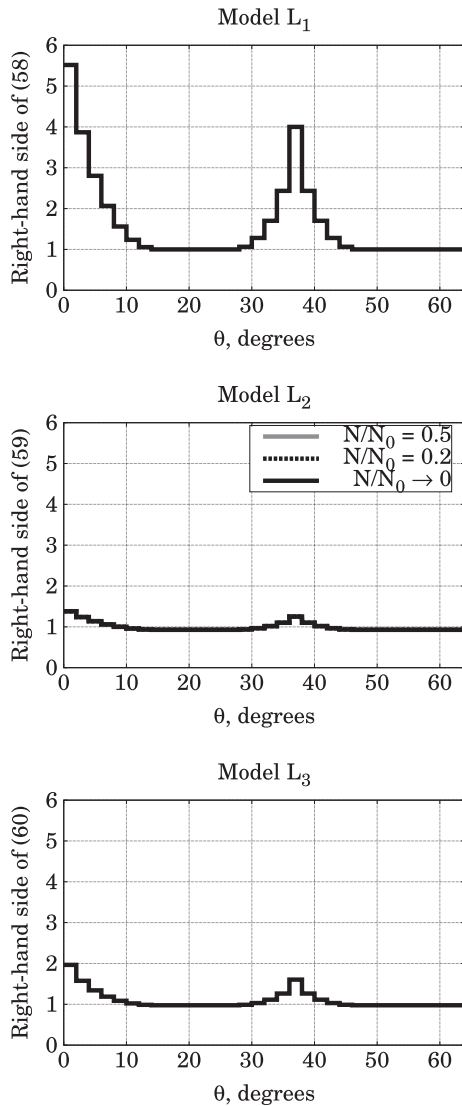


Fig. 25. Right-hand sides of (57)–(59) (specifying boundary lengthening models L_1 , L_2 , L_3) for the grain boundary energy density of Type VI. The right-hand side of (58) is computed for the case when $\lambda = \lambda(N)$ is determined by (56) with $\lambda_{\text{isotr}} = 1.34$, $v(x) \equiv x$.

despite the energy reduction principles. In compliance with [14, Section 2.2] and [13, Section 4.4], the histograms for $\{P_{s,+}^i(N)\}_{i=1}^r$ in Figs. 26 and 27 stay very close to the so-called texture-weighted distribution which is just Mackenzie distribution for general random orientation textures with the cubic lattice symmetry.

3. The boundary lengthening phenomenon makes the length-weighted DDF evolve stronger than the number-weighted DDF for anisotropic boundary energy densities. The isotropic case is trivial: according to Fig. 13, $\rho_l = \rho_n$ does not evolve. As for the Read-Shockley boundary energy densities of Types II–IV, the corresponding Figs. 14–16, 19, and 20 demonstrate that, the greater the cutoff angle, the more the number- and especially length-weighted DDFs increase at low-energy disorientations and, consequently, decrease at high-energy disorientations. By comparing Figs. 15, 16, 19 and 20 with [13, Fig. 5(a)], [14, Fig. 7], [23, Fig. 4(b)], we deduce the following:

- our kinetic approach together with boundary lengthening model L_2 or L_3 gives results similar to the corresponding results of numerical simulations via Monte Carlo and level set techniques as well as via the kinetic model proposed in [14];

Fig. 26. Normalized histograms corresponding to $\{P_{s,+}^i(N)\}_{i=1}^r$, $\{P_{s,-}^i(N)\}_{i=1}^r$, $\{P_{d,1}^i(N)\}_{i=1}^r$, $\{P_{d,2}^i(N)\}_{i=1}^r$ for the grain boundary energy density of Type II and $\lambda = \lambda(N)$ determined by (56) with $\lambda_{\text{isotr}} = 1.34$, $v(x) \equiv x$.

- within the limits of our framework, model L_1 predicts much greater boundary lengthening than obtained from the mentioned large-scale simulations.

Besides, by the use of models L_2 and L_3 , we detect an essential qualitative difference between the DDFs for the boundary energy

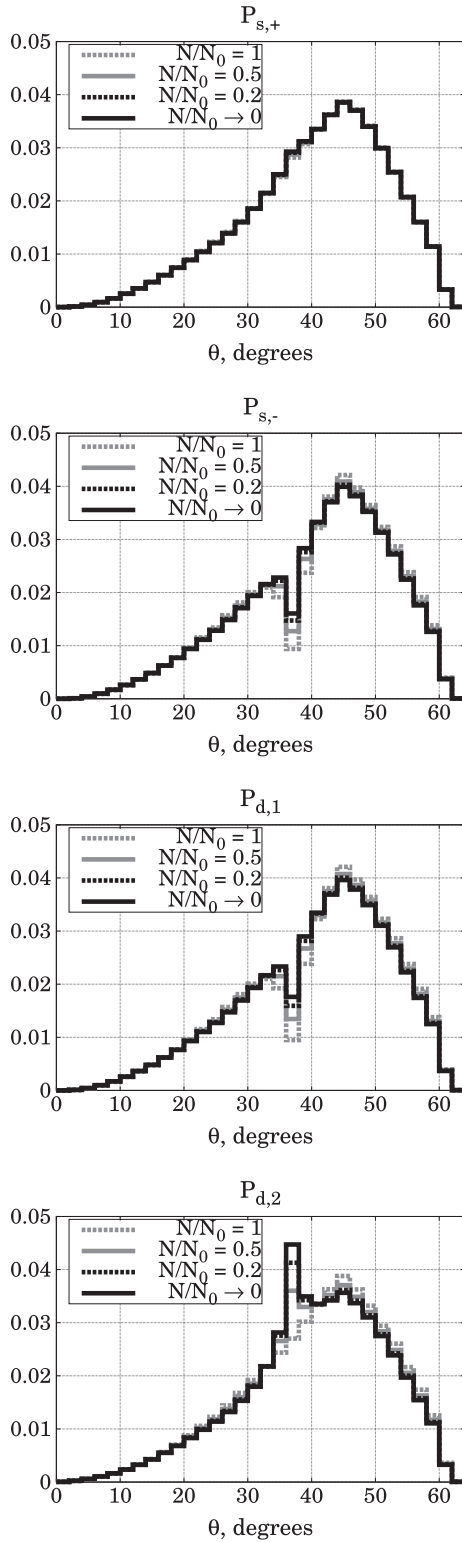


Fig. 27. Normalized histograms corresponding to $\{P_{s,+}^i(N)\}_{i=1}^r$, $\{P_{s,-}^i(N)\}_{i=1}^r$, $\{P_{d,1}^i(N)\}_{i=1}^r$, $\{P_{d,2}^i(N)\}_{i=1}^r$ for the grain boundary energy density of Type VI and $\lambda = \lambda(N)$ determined by (56) with $\lambda_{\text{isotr}} = 1.34$, $v(x) \equiv x$.

densities of Types IV and V. This difference was illustrated and discussed in [23, Section 4.1.2, Fig. 4]. Indeed, comparing Figs. 16 and 20 with Figs. 17 and 21, respectively, also indicates that, for the affine boundary energy density of Type V (having the same cutoff disorientation angle θ_{max} as the Read-Shockley boundary energy

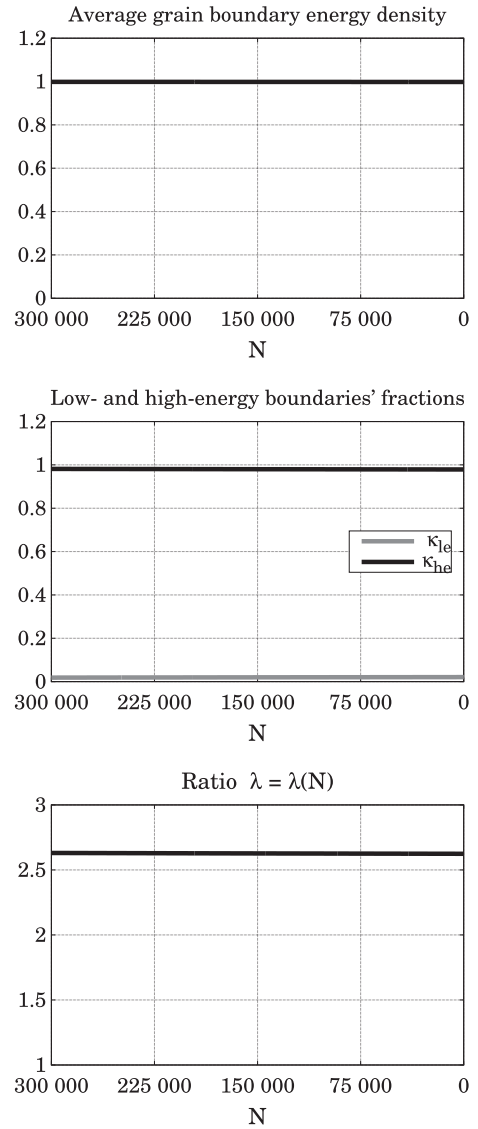


Fig. 28. Evolution of the quantities (54) and (56) for the grain boundary energy density of Type II. In (56), $\lambda_{\text{isotr}} = 1.34$ and $v(x) \equiv x$.

density of Type IV), the number- and especially length-weighted DDFs evolve much faster and reflect a considerably stronger preference for low-energy interfaces. As opposed to models L₂ and L₃, model L₁ shows a significant increase in the length fractions of low-energy interfaces for both of the energy density types (and also for Type III as seen from Fig. 15). Hence, within the limits of our approach, models L₂ and L₃ turn out to produce more adequate results than model L₁. Furthermore, among all the considered energy density types, new peaks of the number- and length-weighted DDFs appear only for Type VI at the intermediate local minimum $\theta = \theta_{V1}$; see Figs. 18 and 22. Unlike the fiber-texture case investigated in [18,1], peaks at $\theta = 0$ do not form.

4. Figs. 28 and 29 illustrate the following property. Suppose that the Read-Shockley boundary energy density of Type II is replaced with its modification in the form of the boundary energy density of Type VI (having an additional local minimum at $\theta = \theta_{V1} > \theta_{II}$). Then the average energy density $\bar{\gamma} = \bar{\gamma}(N)$ and fraction $\kappa_{\text{he}} = \kappa_{\text{he}}(N)$ of high-energy boundaries take smaller values and decrease a little bit faster with decreasing N , while the fraction $\kappa_{\text{le}} = \kappa_{\text{le}}(N)$ of low-energy boundaries takes greater values and increases a little bit faster with decreasing N .

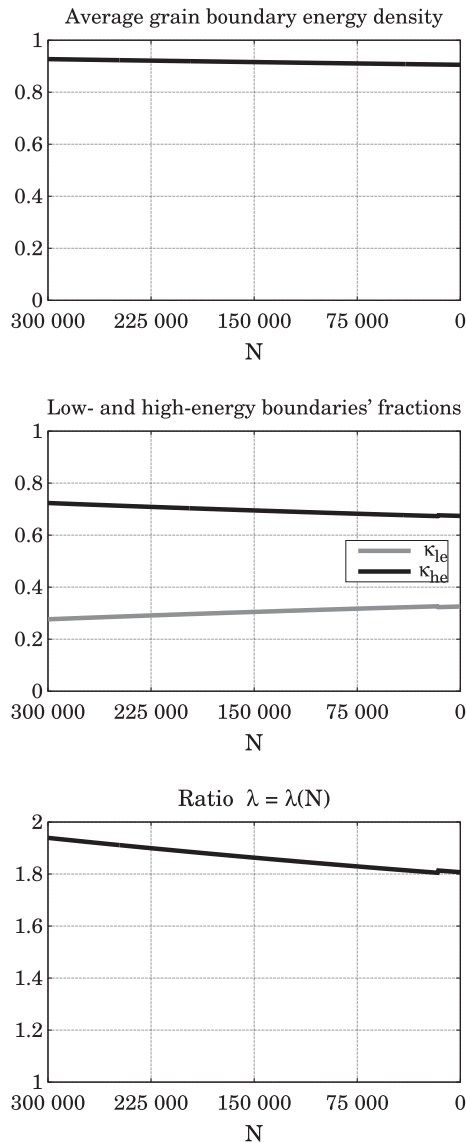


Fig. 29. Evolution of the quantities (54) and (56) for the grain boundary energy density of Type VI. In (56), $\lambda_{\text{isotr}} = 1.34$ and $v(x) \equiv x$.

10. Concluding remarks

In this paper, a Boltzmann-type kinetic modeling approach for two-dimensional polycrystalline grain growth was proposed. This was an extension of the fiber-texture framework developed in [1] to the case of general textures with anisotropic grain boundary energy densities depending only on the disorientation angle. The number-weighted disorientation distribution function was approximated numerically by solving a specific system of ordinary differential equations, where the time variable was replaced with the time-decreasing total number of grain boundaries. These equations were initially derived in a discretized form with respect to the disorientation variable. Besides, in order to obtain their terms describing the influence of topological transitions on the number-weighted disorientation distribution function, a collection of auxiliary a priori distributions was used. The latter concerned possible disorientations of grain boundaries connected in a triple junction and were numerically constructed for the technologically important subcase of the cubic lattice symmetry taking place in a wide class of metals and alloys. As in [1,14], the ratio of the

length- and number-weighted disorientation distribution functions was estimated via boundary lengthening models. Three variants of such models were compared with each other in terms of the obtained numerical results.

Unlike the evolving number- and length-weighted disorientation distributions, the mentioned a priori distributions have to be constructed only once for the cubic or any other particular lattice symmetry and depend on none of such quantities as the grain boundary energy density, ratio of the neighbor switchings' rate to the grain disappearances' rate, initial number of grain boundaries, initial number- and length-weighted disorientation distributions.

The numerical results obtained via the presented approach showed good agreement with the corresponding large-scale simulation results from [14,23].

Moreover, the developed framework is based on solving a system of kinetic ordinary differential equations and, therefore, a priori more computationally efficient than large-scale simulation methods.

As a future perspective, it is worth investigating to extend the proposed general-texture approach by introducing the intragranular stored energy variable into the kinetic model, which may help to investigate primary recrystallization as well as grain growth. Then, in addition to neighbor switchings and grain disappearances, one new type of topological transitions has to be taken into account. It arises only in the presence of differences between grains' stored energies, when a vertex, i.e., a junction of grain boundaries, collides with the interior of some other boundary; see [33–35].

Acknowledgements

I. Y. was supported in part by National Science Foundation grant DMS-1056821 and Russian state subsidy for applied scientific research 14.607.21.0091. M. E. was supported in part by National Science Foundation grant DMS-1056821.

References

- [1] I. Yegorov, C.E. Torres, M. Emelianenko, A Boltzmann-type kinetic model for misorientation distribution functions in two-dimensional fiber-texture polycrystalline grain growth, *Acta Mater.* 109 (2016) 230–247.
- [2] V. Randle, G. Owen, Mechanisms of grain boundary engineering, *Acta Mater.* 54 (2006) 1777–1783.
- [3] U. Krupp, W.M. Kane, X. Liu, O. Dueber, C. Laird, C.J. McMahon Jr., The effect of grain-boundary-engineering-type processing on oxygen-induced cracking of IN718, *Mater. Sci. Eng., A* 349 (2003) 213–217.
- [4] B. Alexandreanu, G.S. Was, The role of stress in the efficacy of coincident site lattice boundaries in improving creep and stress corrosion cracking, *Scripta Mater.* 54 (2006) 1047–1052.
- [5] G. Gupta, B. Alexandreanu, G.S. Was, Grain boundary engineering of ferritic-martensitic alloy T91, *Metall. Mater. Trans.* 35A (2004) 717–719.
- [6] T. Furuhashi, T. Maki, Grain boundary engineering for superplasticity in steels, *J. Mater. Sci.* 40 (2005) 919–926.
- [7] M. Kurban, U. Erb, K.T. Aust, A grain boundary characterization study of boron segregation and carbide precipitation in alloy 304 austenitic stainless steel, *Scripta Mater.* 54 (2006) 1053–1058.
- [8] W. Smith, J. Hashemi, *Foundations of Materials Science and Engineering*, McGraw-Hill, London, 2009.
- [9] G. Gottstein, L.S. Shvindlerman, *Grain Boundary Migration in Metals: Thermodynamics, Kinetics, Applications*, Taylor & Francis Group, Boca Raton, 2010.
- [10] E.A. Holm, G.N. Hassold, M.A. Miodownik, On misorientation distribution evolution during anisotropic grain growth, *Acta Mater.* 49 (2001) 2981–2991.
- [11] D. Moldovan, D. Wolf, S.R. Phillpot, A.J. Haslam, Mesoscopic simulation of two-dimensional grain growth with anisotropic grain-boundary properties, *Philos. Mag.* 82 (7) (2002) 1271–1297.
- [12] M. Upanyu, G.N. Hassold, A. Kazaryan, E.A. Holm, Y. Wang, B. Patton, D.J. Srolovitz, Boundary mobility and energy anisotropy effects on microstructural evolution during grain growth, *Interface Sci.* 10 (2) (2002) 201–216.
- [13] J. Gruber, H.M. Miller, T.D. Hoffmann, G.S. Rohrer, A.D. Rollett, Misorientation texture development during grain growth. Part I: Simulation and experiment, *Acta Mater.* 57 (2009) 6102–6112.

- [14] J. Gruber, G.S. Rohrer, A.D. Rollett, Misorientation texture development during grain growth. Part II: Theory, *Acta Mater.* 58 (2010) 14–19.
- [15] G.S. Rohrer, J. Gruber, A.D. Rollett, A model for the origin of anisotropic grain boundary character distributions in polycrystalline materials, in: A.D. Rollett (Ed.), *Applications of Texture Analysis*, Ceram. Trans., vol. 201, John Wiley & Sons, Hoboken, New Jersey, 2009.
- [16] S.J. Dillon, G.S. Rohrer, Mechanism for the development of anisotropic grain boundary character distributions during normal grain growth, *Acta Mater.* 57 (1) (2009) 1–7.
- [17] A. Kazaryan, Y. Wang, S.A. Dregia, B.R. Patton, Grain growth in anisotropic systems: comparison of effects of energy and mobility, *Acta Mater.* 50 (2002) 2491–2502.
- [18] N. Moelans, F. Spaepen, P. Wollants, Grain growth in thin films with a fiber texture studied by phase-field simulations and mean field modeling, *Philos. Mag.* 90 (1–4) (2010) 501–523.
- [19] D. Kinderlehrer, J. Lee, I. Livshits, A. Rollett, S. Ta'asan, Mesoscale simulation of grain growth, *Mater. Sci. Forum* 467–470 (2004) 1057–1062.
- [20] D. Kinderlehrer, I. Livshits, G.S. Rohrer, S. Ta'asan, P. Yu, Mesoscale simulation of the evolution of the grain boundary character distribution, *Mater. Sci. Forum* 467–470 (2004) 1063–1068.
- [21] D. Kinderlehrer, I. Livshits, S. Ta'asan, A variational approach to modeling and simulation of grain growth, *SIAM J. Sci. Comput.* 28 (5) (2006) 1694–1715.
- [22] K. Barmak, M. Emelianenko, D. Golovaty, D. Kinderlehrer, S. Ta'asan, A new perspective on texture evolution, *Int. J. Numer. Anal. Model.* 5 (2008) 93–108.
- [23] M. Elsey, S. Esedoglu, P. Smereka, Simulations of anisotropic grain growth: efficient algorithms and misorientation distributions, *Acta Mater.* 61 (6) (2013) 2033–2043.
- [24] H. Hallberg, Influence of anisotropic grain boundary properties on the evolution of grain boundary character distribution during grain growth—A 2D level set study, *Model. Simul. Mater. Sci. Eng.* 22 (8) (2014) 085005.
- [25] K. Chang, N. Moelans, Effect of grain boundary energy anisotropy on highly-textured grain structures studied by phase field simulations, *Acta Mater.* 64 (2014) 443–454.
- [26] D. Weygand, Y. Brechet, J. Lepinoux, A vertex dynamics simulation of grain growth in two dimensions, *Philos. Mag.* B 78 (4) (1998) 329–352.
- [27] R. Henseler, B. Niethammer, F. Otto, A reduced model for simulating grain growth, in: *Free Boundary Problems 2004*, ISNM International Series of Numerical Mathematics, vol. 147, pp. 177–187.
- [28] C.E. Torres, M. Emelianenko, D. Golovaty, D. Kinderlehrer, S. Ta'asan, Numerical analysis of the vertex models for simulating grain boundary networks, *SIAM J. Appl. Math.* 75 (2) (2015) 762–786.
- [29] O. Engler, V. Randle, *Introduction to Texture Analysis: Macrotexture, Microtexture, and Orientation Mapping*, Taylor and Francis Group, Boca Raton, 2010.
- [30] H. Grimmer, Disorientations and coincidence rotations for cubic lattices, *Acta Crystallogr. A* A30 (1974) 685–688.
- [31] A. Heinz, P. Neumann, Representation of orientation and disorientation data for cubic, hexagonal, tetragonal and orthorhombic crystals, *Acta Crystallogr. A* A47 (1991) 780–789.
- [32] A.P. Sprague, B.R. Patterson, S. Grandhi, Topological characteristics of two-dimensional grain growth—simulation and analysis, *Metall. Mater. Trans. A* 41 (3) (2010) 592–602.
- [33] K. Piekos, J. Tarasiuk, K. Wierzbanski, B. Bacroix, Recrystallization study using two-dimensional vertex model, *Arch. Metall. Mater.* 50 (1) (2005) 131–138.
- [34] K. Piekos, J. Tarasiuk, K. Wierzbanski, B. Bacroix, Stochastic vertex model of recrystallization, *Comput. Mater. Sci.* 42 (2008) 36–42.
- [35] K. Piekos, J. Tarasiuk, K. Wierzbanski, B. Bacroix, Generalized vertex model of recrystallization—application to polycrystalline copper, *Comput. Mater. Sci.* 42 (2008) 584–594.